J. Fluid Mech. (1993), *vol.* 251, *pp.* 315–353

Axially invariant laminar flow in helical pipes with a finite pitch

By SHIJIE LIU AND JACOB H. MASLIYAH
Department of Chemical Engineering, University of Alberta, Edmonton, Canada T6G 2G6

(Received 28 November 1991 and in revised form 16 December 1992)

Steady axially invariant (fully developed) incompressible laminar flow of a Newtonian fluid in helical pipes of constant circular cross-section with arbitrary pitch and arbitrary radius of coil is studied. A loose-coiling analysis leads to two dominant parameters, namely Dean number, $Dn = Re\lambda^{\frac{1}{2}}$, and Germano number, $Gn = Re\eta$, where Re is the Reynolds number, λ is the normalized curvature ratio and η is the normalized torsion. The Germano number is embedded in the body-centred azimuthal velocity which appears as a group in the governing equations. When studying Gn effects on the helical flow in terms of the secondary flow pattern or the secondary flow structure viewed in the generic (non-orthogonal) coordinate system of large Dn, a third dimensionless group emerges, $\gamma = \eta/(\lambda Dn)^{\frac{1}{2}}$. For $Dn < 20$, the group $\gamma^* = Gn\,Dn^{-2} = \eta/(\lambda Re)$ takes the place of γ.

Numerical simulations with the full Navier–Stokes equations confirmed the theoretical findings. It is revealed that the effect of torsion on the helical flow can be neglected when $\gamma \leqslant 0.01$ for moderate Dn. The critical value for which the secondary flow pattern changes from two vortices to one vortex is $\gamma^* > 0.039$ for $Dn < 20$ and $\gamma > 0.2$ for $Dn \geqslant 20$. For flows with fixed high Dean number and λ, increasing the torsion has the effect of changing the relative position of the secondary flow vortices and the eventual formation of a flow having a Poiseuille-type axial velocity with a superimposed swirling flow. In the orthogonal coordinate system, however, the secondary flow generally has two vortices with sources and sinks. In the small-γ limit or when Dn is very small, the secondary flow is of the usual two-vortex type when viewed in the orthogonal coordinate system. In the large-γ limit, the appearance of the secondary flow in the orthogonal coordinate system is also two-vortex like but its orientation is inclined towards the upper wall. The flow friction factor is correlated to account for Dn, λ and γ effects for $Dn \leqslant 5000$ and $\gamma < 0.1$.

1. Introduction

Laminar flow in helical pipes of constant circular cross-section is of practical importance in many branches of engineering in which pipe systems are used for transport and treatment of gases and liquids. The problem of the flow in a toroidal pipe, i.e. a helical pipe with a zero pitch, was dealt with extensively and drew great interest after the initial work by Dean (1927, 1928). Most of the studies dealing with laminar flow in a torus concentrated on the limiting case of the loose coiling where $1/R_c = a/R'_c$ approaches zero. R'_c is the radius of the coil and a is the radius of the pipe. The mathematical limit of this case is of great interest as the flow is governed by a single parameter, namely the Dean number, $D = (G\rho a^3/\mu^2)(2/R_c)^{\frac{1}{2}}$ with G the axial pressure gradient, ρ fluid density and μ the dynamic viscosity of the fluid. Several different versions of Dean number have been defined. Since D involves the pressure gradient G,

it is hardly an appropriate physical controlling parameter to be considered for a flow problem. A more common version of the Dean number is defined by $Dn = Re/R_c^{\frac{1}{2}}$, where Re is the Reynolds number. For details, the reader is referred to the review articles dealing with the flow in a torus by Nandakumar & Masliyah (1986) and more recently, Berger (1991).

One of the interesting features of the flow through a toroidal pipe (torus) has been that dual or more solutions appear if Dn exceeds a certain critical value. It has been a challenge to compute the secondary solutions. The stationary four-vortex solution with the symmetry prescribed was obtained accidentally by Dennis & Ng (1982) and Yanase, Goto & Yamamoto (1989); through gradual geometrical change by Nandakumar & Masliyah (1982) and Daskopoulos & Lenhoff (1989) and with the method of continuation by Yang & Keller (1986). Nandakumar & Masliyah (1982) documented the flow properties in terms of Dn and R_c. Additional solutions are also presented by Yang & Keller (1986) and Daskopoulos & Lenhoff (1989) without confirming each other. The characteristics of the developing flow are still unknown. The stability of flows in a torus has been studied by Yanase *et al.* (1989) and Daskopoulos & Lenhoff (1989). Yanase *et al.* (1989) found that both two- and four-vortex flows are stable when symmetry is imposed while only the two-vortex flow is stable when no symmetry is imposed. Daskopoulos & Lenhoff (1989) found that only two- and four-vortex flows are stable when symmetry is imposed.

Laminar flow in helical pipes of finite pitch has been treated less extensively. Starting with Truesdell & Adler (1970), it was suggested that an appropriate approximation might be obtained by replacing the curvature for a toroidal pipe by the curvature for the helical pipe under consideration, at least for coils of small pitch. This was continued by Manlapaz & Churchill (1980), who assumed the effects of non-orthogonality to be negligible in the limit of small pitch. Non-orthogonal helical systems were studied by Wang (1981) and Murata *et al.* (1981). Owing to the non-orthogonality of the coordinates, problems may arise in the interpretation of their results. To avoid the complexity associated with the non-orthogonal helical coordinate system as noted by Murata *et al.* (1981), Germano (1982, 1989) introduced a helical orthogonal coordinate system.

The complexity of the system drew many different explanations of the torsion effect. Often apparently opposing results were obtained. Both Tuttle (1990) and Xie (1990) attempted to resolve the controversy. Xie (1990) worked on the non-orthogonal coordinate system alone. Tuttle (1990) attempted to relate the orthogonal and the non-orthogonal coordinates and succeeded in resolving the controversy. Wang (1981) found that for $Re = O(1)$ the torsion effect on the secondary flow is of $O(\eta)$. However, Murata *et al.* (1981) and Tuttle (1990) found that the torsion effect on the secondary flow is of $O(\lambda\eta)$. Germano (1982) stated that the torsion effect is of second order. In a later study, Germano (1989) found that the pipe torsion influences the secondary flow through the dimensionless group $\eta\, Re$ (denoted by T in his paper) for a non-circular geometry. For a circular geometry, Germano stated that no pure torsion effect at any order is to be expected. Kao (1987) found that $\eta(2\lambda)^{-\frac{1}{2}}$ is a controlling parameter determining whether the torsion can exert a $1\frac{1}{2}$-order effect, and that for $\lambda \geqslant 0.4$ the nonlinear interactions become important.

Although the order of the torsion effect on the main flow has been resolved by Tuttle (1990), the representation of the secondary flow is controversial. Tuttle (1990) stated that the (pseudo-) secondary flow stream function is preferable. He argued that the non-orthogonal coordinate system is generic to the helical pipe. Earlier, Murata *et al.* (1981) and Kao (1987) had stated that no stream-function-like property exists and the

orthogonal secondary flow velocity vector is the only appropriate choice since it is normal to the axial flow. However, the orthogonal secondary velocity vector plots are not very appropriate in describing the axially invariant (fully developed) secondary flows since, as Tuttle (1990) noted, they contain sources and sinks. Wang (1981) was able to define a (pseudo-) secondary flow stream function using the physical covariant velocity components in the non-orthogonal (generic) coordinate system. This pseudo-secondary flow stream function was used by Germano (1982, 1989) and by Tuttle (1990). However, Germano (1982, 1989) preferred to present the secondary flow using the orthogonal velocity vectors. Wang (1981) and Tuttle (1990) presented the secondary flow using the pseudo-secondary flow stream function. Tuttle (1990) further stated that the pseudo-secondary flow stream function is indeed a stream function.

For $Re = O(1)$, Wang (1981) found that the two recirculating cells become one when $\eta/\lambda\, Re \geqslant \frac{1}{24}$. The two recirculating cells (vortices) were in an up-and-down position when the helix axis is vertical. Kao's attempt to compute four-vortex-type solutions failed. The state of understanding of laminar flow in helical pipes with finite pitch is relatively immature especially for large Reynolds number flows, where investigations should be conducted.

In this study, the separation method (Liu 1992; Liu & Masliyah 1993) is used to solve the problem of laminar Newtonian fluid flows in helical pipes having a non-zero pitch. The flow simulations are made using the Navier–Stokes equations constructed from the orthogonal helical coordinates after Germano (1982). A scale analysis is performed for the limiting case of loose coiling and the dominant dimensionless groups are identified. The argument over the representation of the secondary flow is also addressed.

2. Mathematical formulation

Figure 1 shows a sketch of a helical coil and the orientations of the reference systems useful in describing the helical pipe. A helical system can be established in reference to the master Cartesian coordinate system $x(x_1, x_2, x_3)$ and the local vectors originated on the generic curve of the helix as follows:

$$\boldsymbol{R} = (R_c \cos\varphi, R_c \sin\varphi, bs), \tag{1}$$

$$\boldsymbol{T} = \mathrm{d}\boldsymbol{R}/\mathrm{d}s = (-(\lambda R_c)^{\frac{1}{2}} \sin\varphi, (\lambda R_c)^{\frac{1}{2}} \cos\varphi, b), \tag{2}$$

$$\boldsymbol{N} = \frac{1}{\lambda}\frac{\mathrm{d}\boldsymbol{T}}{\mathrm{d}s} = (-\cos\varphi, -\sin\varphi, 0), \tag{3}$$

$$\boldsymbol{B} = \boldsymbol{T} \times \boldsymbol{N} = (b\sin\varphi, -b\cos\varphi, (\lambda R_c)^{\frac{1}{2}}), \tag{4}$$

$$\varphi = s/[R_c^2 + (H/2\pi)^2]^{\frac{1}{2}}, \tag{5}$$

where $b = (\eta H/2\pi)^{\frac{1}{2}}$; $\boldsymbol{R}$ is the global coordinate vector at the point of consideration O on the generic curve; the generic curve is the track of a particle moving along the centre of the helical pipe; T (shown as s in figure 1), $\boldsymbol{N}$ and $\boldsymbol{B}$ are the tangential, normal and binormal to the generic curve at the point of consideration on the generic curve, respectively; s is the dimensionless curve length parameter along the generic curve, $s = s'/a$; λ and η are the dimensionless curvature ratio and torsion, respectively; R_c and H are the dimensionless radius of curvature and the dimensionless pitch for the helix, respectively, $R_c = R_c'/a$ and $H = H'/a$. The orthogonality of a helical coordinate system can be achieved by simply rotating the basis formed by the Frenet frame $\boldsymbol{B}$ and $\boldsymbol{N}$ (the physical plane of $\boldsymbol{B} \times \boldsymbol{N}$ will be conserved) around the s-axis.

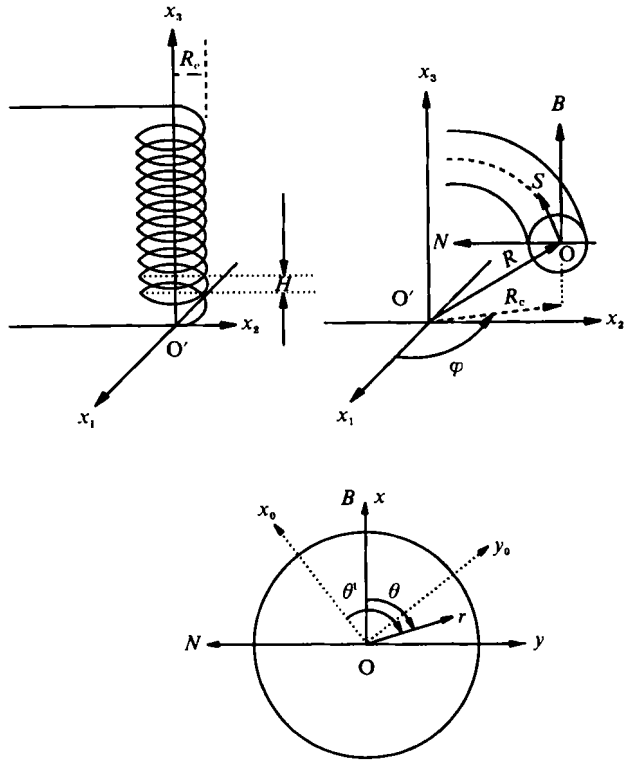

FIGURE 1. Helical coil and its reference systems.

A given point in the pipe can be mapped to the master Cartesian system through

$$\boldsymbol{x} = \boldsymbol{R} + r\cos\theta \boldsymbol{N} + r\sin\theta \boldsymbol{B}. \tag{6}$$

The metrics for the transition are given by

$$g_{ij} = \frac{\partial x_k}{\partial q_i}\frac{\partial x_k}{\partial q_j}, \tag{7}$$

where $q_1 = s$, $q_2 = r$, $q_3 = \theta^t$ and $\theta^t = \theta + f(s)$. The basic equations of curve theory

$$\mathrm{d}N/\mathrm{d}s = \eta B - \lambda T, \tag{8}$$

$$\mathrm{d}B/\mathrm{d}s = -\eta N, \tag{9}$$

can be applied to derive the helical coordinate system, where the curvature ratio

$$\lambda = \frac{R_c}{R_c^2 + (H/2\pi)^2} \tag{10}$$

and the torsion is defined by

$$\eta = \frac{(H/2\pi)}{R_c^2 + (H/2\pi)^2}. \tag{11}$$

By forcing $g_{ij} = 0$, for all mutations of i and j when $i \neq j$, with a suitable choice for the function $f(s)$, the helical coordinate system (s, r, θ^t) is set to be orthogonal. The metrics of the coordinate system can then be obtained as

$$h_1 = g_{11}^{\frac{1}{2}} = 1 + \lambda r\sin\theta, \quad h_2 = g_{22}^{\frac{1}{2}} = 1, \quad h_3 = g_{33}^{\frac{1}{2}} = r, \tag{12}$$

where $\theta^t = \theta + \eta s$, and (s, r, θ^t) and its corresponding rectangular coordinates (s, x_0, y_0) are orthogonal.

The governing equations are first derived in the orthogonal system (s, r, θ^t) and transformed to the non-orthogonal system (s, r, θ), leaving the velocity components untouched. The transformation is necessary to eliminate the s-dependent coefficients and variables ($\theta^t - \eta s$ always appears in place of θ). This would allow an axially invariant solution to be realizable if exists. It should be noted that the above equations used dimensionless quantities. To work with the flow problem, the variables are non-dimensionalized in the following manner:

$$s = \frac{s'}{a}, \quad r = \frac{r'}{a}, \quad t = \nu t' a^{-2}, \quad u = \frac{u'}{2U}, \quad v = \frac{v'}{2U}, \quad p = \frac{Re\, p'}{4\rho U^2}, \quad Re = \frac{2aU}{\nu},$$

where a is the radius of the pipe, U is the average axial velocity, t is time, ν is the kinematic viscosity, u is the axial velocity component (orthogonal s-directional component), v is the radial velocity component (r-direction), w is the angular velocity component (orthogonal θ^t-directional component), Re is the Reynolds number and p is the pressure. The primed variables are the dimensional quantities. For simplicity, we will use the non-dimensional variables hereafter.

The final governing flow equations after all necessary substitution and rearrangement are as follows. The continuity equation is

$$\frac{1}{h_1}\left(\frac{\partial u}{\partial s} - \eta \frac{\partial u}{\partial \theta}\right) + \frac{1}{r h_1}\frac{\partial (r h_1 v)}{\partial r} + \frac{1}{r h_1}\frac{\partial (h_1 w)}{\partial \theta} = 0, \tag{13}$$

where h_1 is the metric coefficient in the axial direction (s-direction),

$$h_1 = 1 + \lambda r \sin\theta. \tag{14}$$

The momentum and energy equations are

$$(\mathrm{M} + d_\phi)\,\phi = S_\phi \tag{15a}$$

where the momentum or energy operator M is defined by

$$\mathrm{M}\phi = \frac{\partial \phi}{\partial t} + \frac{2\eta}{h_1^2}\frac{\partial^2 \phi}{\partial s\, \partial \theta} + \frac{1}{h_1}\frac{\partial}{\partial s}\left[\left(Re\, u - \lambda \eta r \frac{\cos\theta}{h_1^2}\right)\phi - \frac{1}{h_1}\frac{\partial \phi}{\partial s}\right]$$
$$+ \frac{1}{r h_1}\frac{\partial}{\partial r}\left[r h_1 \left(Re\, v\phi - \frac{\partial \phi}{\partial r}\right)\right] + \frac{1}{r h_1}\frac{\partial}{\partial \theta}\left[Re\,(h_1 w - \eta r u)\,\phi - \frac{h_1}{r}\left(1 + \frac{\eta^2 r^2}{h_1^2}\right)\frac{\partial \phi}{\partial \theta}\right], \tag{15b}$$

where ϕ stands for any velocity component or the temperature. The individual equations are obtained by specification of the velocity component ϕ, the extra diagonal term d_ϕ and the source term S_ϕ:

s-momentum: $\phi = u$

$$d_\phi = \frac{v \sin\theta + w \cos\theta}{h_1}\lambda\, Re + \frac{\lambda^2}{h_1^2}, \tag{16a}$$

$$S_\phi = -\frac{1}{h_1}\left(\frac{\partial p}{\partial s} - \eta \frac{\partial p}{\partial \theta}\right)$$
$$+ \frac{\lambda}{h_1^2}\left[2\sin\theta\left(\frac{\partial v}{\partial s} - \eta \frac{\partial v}{\partial \theta}\right) + 2\cos\theta\left(\frac{\partial w}{\partial s} - \eta \frac{\partial w}{\partial \theta}\right) + \frac{\eta \cos\theta}{h_1} v - \frac{\lambda r + \sin\theta}{h_1}\eta w\right]; \tag{16b}$$

r-momentum: $\phi = v$

$$d_\phi = \frac{1+2h_1\lambda r\sin\theta}{r^2h_1^2}, \tag{17a}$$

$$S_\phi = -\frac{\partial p}{\partial r} + Re\left(\frac{\lambda\sin\theta}{h_1}u^2 + \frac{w^2}{r}\right) - \frac{2\lambda\sin\theta}{h_1^2}\left(\frac{\partial u}{\partial s} - \eta\frac{\partial u}{\partial\theta}\right) + \frac{\lambda\eta\cos\theta}{h_1^3}u - \frac{2}{r^2}\frac{\partial w}{\partial\theta} - \frac{2h_1-1}{rh_1^2}\lambda\cos\theta w; \tag{17b}$$

θ-momentum: $\phi = w$

$$d_\phi = Re\frac{v}{r} + \frac{1}{h_1^2}\left(\lambda^2 + \frac{2h_1-1}{r}\right), \tag{18a}$$

$$S_\phi = -\frac{\partial p}{\partial\theta} + Re\frac{\lambda\cos\theta}{h_1}u^2 - \frac{2\lambda\cos\theta}{h_1^2}\left(\frac{\partial u}{\partial s} - \eta\frac{\partial u}{\partial\theta}\right) - \frac{\lambda r+\sin\theta}{h_1^2}\lambda\eta u + \frac{3h_1-1}{r^2h_1^2}\frac{\partial v}{\partial\theta} + \frac{\lambda\cos\theta}{rh_1^2}v. \tag{18b}$$

The boundary is defined by the pipe wall. Although it would be preferable for a numerical scheme with a polar coordinate system to have a condition set at the centre of the pipe, the centreline of the pipe is simply an interior point in the computational domain and need not be treated differently. The boundary and necessary conditions are

$$\left.\begin{aligned} &u = v = w = 0 \quad \text{at} \quad r = 1 \quad \text{for all } \theta, \\ &p = 0 \quad \text{at one reference point of choice,} \end{aligned}\right\} \tag{19}$$

$$\frac{\int_0^{2\pi}\mathrm{d}\theta\int_0^1 ru\,\mathrm{d}r}{\pi} = \tfrac{1}{2} \quad \text{(from the non-dimensionalization).} \tag{20}$$

When the flow reaches the fully developed (i.e. axially invariant) stage, the generic transverse velocity field (v, ξ) can be represented by a field potential, ψ, as follows:

$$rh_1 v = -\partial\psi/\partial\theta, \tag{21a}$$

$$h_1\xi = h_1 w - \eta ru = \partial\psi/\partial r, \tag{21b}$$

where ξ is the body-centred azimuthal velocity, or the physical covariant velocity in the azimuthal direction of the generic (non-orthogonal) helical coordinate system (s, r, θ). As for ordinary two-dimensional flows, the field scalar quantity ψ can be called the pseudo-secondary flow stream function. Confirmation of ψ as a stream function is given by Tuttle (1990). To compute ψ, we integrate equation (21 b) after the velocity field is obtained. The iso-ψ lines show a complete picture of the secondary flow viewed in the generic coordinate system (s, r, θ). We shall call the iso-ψ contour plot the secondary flow pattern hereafter.

The presentations of the numerical simulations are based on the (r, θ)- or (x, y)-plane with the orientation shown in figure 1 as the cross-section of the pipe. The non-orthogonal (r, θ)-plane is used simply because it is easy to locate along the pipe and the flow in the pipe is invariant with axial distance if the pipe is long enough.

3. Loose-coiling analysis

The formulation of the flow in a helical pipe indicates that there are three dimensionless parameters involved, namely the curvature ratio λ, the torsion η and the

Reynolds number Re. To identify the dominant parameters, we consider loosely coiled pipes and flow at high Reynolds number, i.e.

$$\lambda \to 0 \quad \text{and} \quad \eta \to 0, \quad \text{while} \quad Re \to +\infty, \quad \lambda \neq 0.$$

The above loose-coiling conditions can be obtained by having either a large radius of coil R_c or a large pitch H. Under the above conditions, we can rearrange the governing equations to obtain the dominant parameters. Let us introduce the following rescaled velocity field:

$$u_1 = u, \quad u_2 = Re\, v, \quad u_3 = Re\, w, \quad P = Re\, p.$$

The above rescaling is necessary since, for a smaller λ, the secondary flow field is weaker for a given main flow, i.e. Re = fixed. For a fixed secondary flow and $\lambda \to 0$, $Re \to \infty$, the above rescaling can make the new secondary flow field variables comparable with the main flow field variables.

In this study, our focus is on axially invariant flows. Hence, we omit the axial variation and note that the normalized pressure gradient is directly related to the friction factor as follows:

$$f Re = -4\frac{\partial p}{\partial s} = -\frac{a\, Re}{\rho U^2}\frac{\partial p'}{\partial s'}, \tag{22}$$

where f is the Fanning friction factor.

For $\lambda \to 0$, $\eta \to 0$ and $Re \to +\infty$, we obtain the following equations:

the metrics of the axial axis $\quad h_1 = 1 + \lambda r \sin\theta \to 1$;

continuity
$$\frac{1}{r}\frac{\partial(u_3 - Re\,\eta r u_1)}{\partial\theta} + \frac{1}{r}\frac{\partial(r u_2)}{\partial r} = 0; \tag{23}$$

momentum
$$\mathrm{M}\phi = \frac{\partial\phi}{\partial t} + \frac{1}{r}\frac{\partial}{\partial r}\left[r\left(u_2\phi - \frac{\partial\phi}{\partial r}\right)\right] + \frac{1}{r}\frac{\partial}{\partial\theta}\left[(u_3 - Re\,\eta r u_1)\phi - \frac{1}{r}\frac{\partial\phi}{\partial\theta}\right], \tag{24}$$

s-momentum

r-momentum
$$\phi = u_1, \quad d_\phi = 0, \quad S_\phi = \tfrac{1}{4} f Re, \tag{25}$$

$$\phi = u_2, \quad d_\phi = \frac{1}{r^2}, \quad S_\phi = -\frac{\partial P}{\partial r} + Re^2\lambda \sin\theta u_1^2 + \frac{u_3^2}{r} + Re\,\lambda\eta\cos\theta u_1 - \frac{2}{r^2}\frac{\partial u_3}{\partial\theta}, \tag{26}$$

θ-momentum

$$\phi = u_3, \quad d_\phi = \frac{u_2}{r} + \frac{1}{r^2}, \quad S_\phi = -\frac{\partial P}{\partial\theta} + Re^2\lambda\cos\theta u_1^2 - Re(\lambda r + \sin\theta)\lambda\eta u_1 + \frac{2}{r^2}\frac{\partial u_2}{\partial\theta}. \tag{27}$$

From (23)–(27), we can see that four groups emerge; namely $Re\,\eta$, $Re^2\lambda$, $Re\,\eta\lambda$ and $Re\,\lambda^2\eta$. The latter two groups are of lower magnitude for $\lambda \to 0$, $\eta \to 0$ and $Re \to +\infty$, while the magnitudes of $Re\,\eta$ and $Re^2\lambda$ are higher. The first group can be identified as the contribution of the 'twisting' forces in a helical pipe and the second group can be related to the centrifugal forces. We define the first group as the Germano number, Gn, where

$$Gn = Re\,\eta = Re\frac{(H/2\pi)}{R_c^2 + (H/2\pi)^2}. \tag{28}$$

Since the twisting forces that make a rotating fluid element twist or swirl are proportional to $\rho\eta U^2$ and the viscous forces are proportional to μU, it follows that the Germano number Gn is a direct measure of the ratio of the twisting forces to the

viscous forces. In other words, the Germano number is a measure of the torsion effect. When Gn is small enough to be negligible, the helical system reduces to the Dean problem.

We define a generalized Dean number as

$$Dn = Re\,\lambda^{\frac{1}{2}} = Re\left(\frac{R_c}{R_c^2+(H/2\pi)^2}\right)^{\frac{1}{2}}. \tag{29}$$

The parameter Dn is sometimes referred to as Helical number (He) or a modified Dean number in the literature. For simplicity, we will refer to it as the Dean number. In the limiting case of $H = 0$ ($\eta \equiv 0$), Dn becomes exactly the same as the Dean number defined by early investigators. Since the inertia forces are proportional to ρU^2, the centrifugal forces are proportional to $\rho\lambda U^2$ and the viscous forces are proportional to μU, it follows that the square of the Dean number, as it appears in the equations, is a direct measure of the product of the ratio of the centrifugal forces to the viscous forces and the ratio of the inertia forces to the viscous forces. The centrifugal forces make the fluid element move toward the outer wall. The viscous forces are responsible for bringing fluid elements back towards the inner wall. Hence, the Dean number is a measure of the secondary flow strength.

After introducing the Germano number and the generalized Dean number and making the loose coiling assumption, the reduced flow equations become:

continuity
$$\frac{1}{r}\frac{\partial(u_3 - Gn\,ru_1)}{\partial\theta} + \frac{1}{r}\frac{\partial(ru_2)}{\partial r} = 0; \tag{30}$$

momentum
$$\mathrm{M}\phi = \frac{\partial\phi}{\partial t} + \frac{1}{r}\frac{\partial}{\partial r}\left[r\left(u_2\phi - \frac{\partial\phi}{\partial r}\right)\right] + \frac{1}{r}\frac{\partial}{\partial\theta}\left[(u_3 - Gn\,ru_1)\phi - \frac{1}{r}\frac{\partial\phi}{\partial\theta}\right], \tag{31}$$

s-momentum
r-momentum
$$\phi = u_1, \quad d_\phi = 0, \quad S_\phi = \tfrac{1}{4} f Re, \tag{32}$$

$$\phi = u_2, \quad d_\phi = \frac{1}{r^2}, \quad S_\phi = -\frac{\partial P}{\partial r} + Dn^2 \sin\theta u_1^2 + \frac{u_3^2}{r} - \frac{2}{r^2}\frac{\partial u_3}{\partial\theta}, \tag{33}$$

θ-momentum
$$\phi = u_3, \quad d_\phi = \frac{u_2}{r} + \frac{1}{r^2}, \quad S_\phi = -\frac{\partial P}{\partial\theta} + Dn^2 \cos\theta u_1^2 + \frac{2}{r^2}\frac{\partial u_2}{\partial\theta}. \tag{34}$$

Hence, from (30)–(34), we observe that only two newly defined parameters, Gn and Dn, are present in the governing flow equations. It is now obvious that, if the Germano number is negligible, the loosely coiled helical problem reduces to the original Dean problem.

It is of interest to note that the Germano number always appears in the form $(u_3 - Gn\,ru_1)$ as seen from (30)–(34). Since the norms of u_3 and u_1 are functions of Dn, it becomes necessary to relate the Germano number and the Dean number in order to find out when the Germano number is important. We note that

$$Re\,\xi = u_3 - Gn\,ru_1 \tag{35}$$

where ξ is the body-centred azimuthal velocity component. As also noted by Tuttle (1990), ξ is a transverse velocity component defined by pseudo-secondary flow stream function ψ, of (21b). Although ξ is not an orthogonal velocity component, it is nevertheless the momentum/energy advection velocity in the azimuthal direction.

Hence, the importance of Gn is to be deduced from the momentum equations. Applying the M operator as defined by (31) on (35) and making use of (32) and (34), leads to

$$Re\,\mathrm{M}\xi = \mathrm{M}u_3 - Gn\,\mathrm{M}(ru_1) \propto Dn^2 - CGnf\,Re, \tag{36}$$

where C is a constant.

Since the normalized pressure gradient $f\,Re \propto Dn^{\frac{1}{2}}$ for large Dn and negligible torsion effect, see Nandakumar & Masliyah (1986), (36) becomes

$$Re\,\mathrm{M}\xi \propto Dn^2(1 - A_1\,Gn\,Dn^{-\frac{3}{2}}), \tag{37}$$

where A_1 is a constant.

Hence, the importance of Gn for a given Dn becomes obvious from (37). In order for the Germano number to have a noticeable influence on the helical flow field, $Gn\,Dn^{-\frac{3}{2}}$ must be large, its magnitude determined by the flow field simulations. To account for this relative importance, we define a new helical flow group γ

$$\gamma = \frac{Gn}{Dn^{\frac{3}{2}}} = \frac{\eta}{(\lambda Dn)^{\frac{1}{2}}}. \tag{38}$$

It is now clear that the Dean problem becomes a special case of the loose coiling approximation when $\gamma \ll 1$. Note that the analysis is based on the premise that secondary flow is present, i.e. centrifugal forces cannot be neglected. Hence, we would hope to qualitatively describe the helical flow field with the Dean flow (toroidal flow) field in the limit of

$$\lambda \to 0, \quad Re > O(\lambda^{-\frac{1}{2}}) \quad \text{and} \quad \gamma \to 0,$$

where $Re > O(\lambda^{-\frac{1}{2}})$ means that Re is of order greater than $\lambda^{-\frac{1}{2}}$, meaning in turn that the Dean number is large. Here $\gamma \to 0$ means that the Germano number is very small as compared with the Dean number. It is understood that the curvature ratio can be small but not identically zero, at which the pipe is straight.

The expression for γ at large Dn was derived assuming $f\,Re$ to be proportional to $Dn^{\frac{1}{2}}$. The uniqueness of γ in governing the effect of torsion on the helical flow is expected to fail when Dn is small. For very small Dn, the axial pressure gradient is relatively invariant with Dn. Hence, (37) must be reconsidered to reflect the variation of $f\,Re$ with Dn for low Dean number flows.

Using the fact that $f\,Re$ is relatively constant for small Dn flows, (36) becomes

$$Re(M\xi)^* \propto Dn^2(1 - A_1^*\,Gn\,Dn^{-2}), \tag{39}$$

where the asterisk denotes small Dn. Hence for very small Dn, the torsion effect is governed by

$$\gamma^* = \frac{Gn}{Dn^2} = \frac{\eta}{\lambda^{\frac{1}{2}} Dn} = \frac{\eta}{\lambda\,Re}. \tag{40}$$

It is not surprising that for low Dn flows, the parameter γ^* turned out to be the flow transition controlling group as was found by Wang (1981).

For large Dn flows, it is then expected that γ would characterize the transition from a torus-like flow to a swirl-like flow: when γ is small, the secondary flow pattern is torus-like, while for a large γ helical flow, the secondary flow pattern is swirl-like. Such profiles may be found in Wang (1981) and Tuttle (1990) for small Dn flows where γ^* is applicable.

The meaning of γ can be deduced from the above derivations. Here, we look at γ in terms of its original source, body-centred azimuthal velocity ξ. It can be deduced that γ is a measure of the ratio of the swirl strength due to the twisting forces ($\eta r u_1$) to the swirl strength due to the centrifugal forces (u_3). This physical implication of γ makes it clear that when γ is large, the centrifugal force effect becomes less important. Hence,

η	100γ	fRe	$u_{0,0}$	u_{max}	r_{max}	θ_{max}	p_{max}	$-p_{min}$
for $\lambda = 0.01$, $Re = 1000$								
0	0	23.90	0.6306	0.8755	0.6110	1.571	5.348	1.666
0.0001	0.01	23.90	0.6305	0.8756	0.6110	1.570	5.348	1.666
0.001	0.1	23.90	0.6305	0.8756	0.6111	1.567	5.344	1.665
0.002	0.2	23.91	0.6305	0.8756	0.6110	1.562	5.349	1.665
0.005	0.5	23.91	0.6304	0.8755	0.6110	1.549	5.352	1.664
0.01	1	23.92	0.6301	0.8750	0.6111	1.527	5.363	1.660
for $\lambda = 0.0025$, $Re = 2000$								
0	0	23.85	0.6301	0.8783	0.6130	1.571	2.693	0.8251
0.00125	0.25	23.85	0.6301	0.8783	0.6130	1.560	2.694	0.8251
for $\lambda = 0.000625$, $Re = 4000$								
0	0	23.83	0.6300	0.8790	0.6135	1.571	1.349	0.4117
0.0003125	0.125	23.83	0.6300	0.8790	0.6135	1.565	1.349	0.4117

TABLE 1. Helical flow properties for $Dn = 100$, $\gamma \leqslant 0.01$, and $\lambda \leqslant 0.01$

the similarity of the helical flow structure is expected to be related to γ rather than η or Gn when the torsion effect is of concern.

4. Numerical results and discussion

The numerical method used here is the separation method (Liu 1992; Liu & Masliyah 1993). The advantage of this technique is that an m-dimensional problem is divided into m one-dimensional subproblems upon each treatment. The spurious pressure modes are eliminated by a careful nodal and interpolate arrangement. For details, the reader is to refer to Liu & Masliyah (1993). The mesh size used in the computations is n25 × 26fu for $Dn \leqslant 20$ and $Dn = 50$, n25 × 32fu for $20 < Dn \leqslant 1000$, n60 × 40fu for $Dn = 2000$ and n100 × 50fu for $Dn = 5000$, unless otherwise mentioned specifically. Here, n25 × 32fu stands for non-uniform mesh in the radial (r-) direction with 25 mesh points and 32 full domain uniform azimuthal (θ-) directional mesh points. It should be stressed that all the numerical results are based on the governing equations with the full range of λ and η, i.e. no loose coiling is introduced into the governing equations in the numerical simulations.

4.1. *Helical flows with negligible λ and γ*

It was shown theoretically in the previous section for the loose coiling analysis that under the conditions $\lambda \to 0$, $\gamma \to 0$ and $Re > O(\lambda^{-\frac{1}{2}})$, the Dean number ($Dn = Re\,\lambda^{\frac{1}{2}}$) has the dominant effect on the axially invariant flow behaviour. In this section, selected numerical simulations will be made to reveal the significance of Dn.

The solution characteristics for helical pipes with small torsion and small curvature ratio for $Dn = 100$, $\lambda \leqslant 0.01$ and $\gamma \leqslant 0.01$ are shown in table 1. Where $u_{0,0}$ is the axial velocity at the centre of the pipe, u_{max}, r_{max} and θ_{max} are the maximum axial velocity and its location; p_{max} and p_{min} are the maximum and the minimum pressure differences from the pipe centre across the pipe.

It is clear from table 1 that the numerical results show good agreement with the theoretical analysis. The axial pressure gradient fRe, $u_{0,0}$, u_{max}, r_{max} and θ_{max} are relatively constant at a given Dn value despite the changes in Re, λ and η. Owing to scale difference in the pressure and the pseudo-secondary flow stream function, the values of p_{max} and p_{min} presented in table 1 are different as λ changes. Had we rescaled the secondary velocity and pressure fields by multiplying them with $\lambda^{-\frac{1}{2}}$ or Re as was

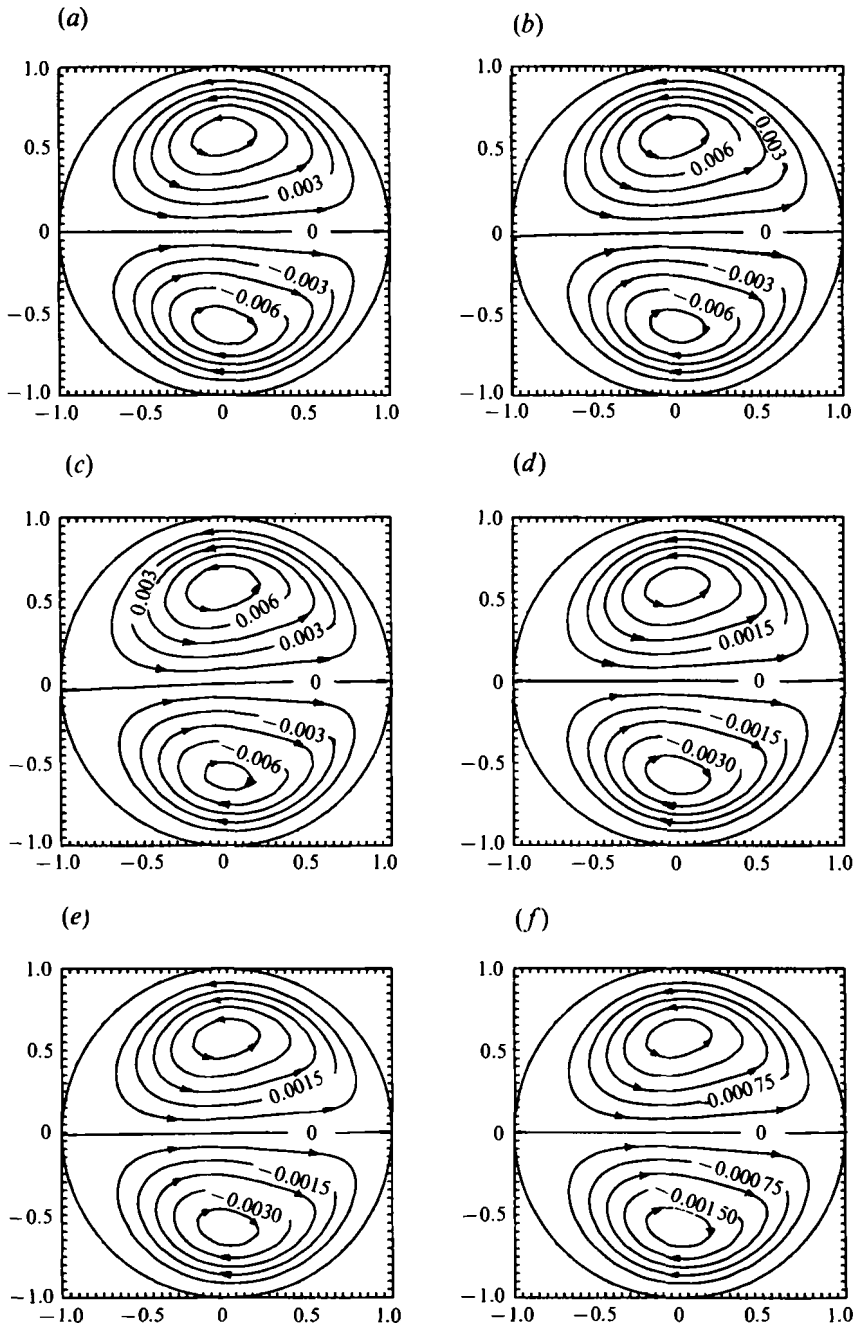

FIGURE 2. Effect of variations of λ and η on secondary flow pattern for $Dn = 100$, $\gamma \leqslant 0.01$ and $\lambda \leqslant 0.01$. (*a*) $\lambda = 0.01$, $\gamma = \eta = 0$; (*b*) $\lambda = 0.01$, $\gamma = \eta = 0.005$; (*c*) $\lambda = 0.01$, $\gamma = \eta = 0.01$; (*d*) $\lambda = 0.0025$, $\gamma = \eta = 0$; (*e*) $\lambda = 0.0025$, $\gamma = 0.0025$, $\eta = 0.00125$; (*f*) $\lambda = 0.000625$, $\gamma = \eta = 0$.

indicated in the loose coiling analysis section, all the quantities in table 1 would look almost identical, irrespective of the individual values of λ and η. This is shown by comparing the product of the pressure and Re for different values of Re.

Under the conditions of loose coiling and small γ, figure 2 shows the secondary flow patterns of the flow in a helical pipe for $Dn = 100$. The range of λ, η and γ is similar

Re	λ	η	100γ	Dn	fRe	u_{max}	Δp_{max}	fRe_{Lit}
1.003	0.2484	0.0198	7*933	0.5	15.98	1.002	0.2111	
2.006	0.2484	0.0198	3*966	1	15.98	1.002	0.4221	
2.207	0.2484	0.0198	3*606	1.1	15.98	1.002	0.4642	
4.013	0.2484	0.0198	1*983	2	15.99	1.001	0.8434	
8.026	0.2484	0.0198	0*9916	4	16.02	0.9992	1.683	
10.03	0.2484	0.0198	1.774	5	16.05	0.9978	2.110	
20.06	0.2484	0.0198	1.254	10	16.40	0.9641	4.128	
50.98	0.1951	0.031	1.479	22.52	17.54	0.9475	7.883	17.54[a]
50.16	0.2484	0.0198	0.7931	25	18.03	0.9288	9.749	
100.3	0.2484	0.0198	0.5609	50	21.27	0.8458	17.68	
200.6	0.2484	0.0198	0.3966	100	25.47	0.7995	31.93	
1003	0.01	0	0	100.3	23.89	0.8753	7.028	23.92[c]
1229	0.01	0	0	122.9	25.47	0.8745	8.482	26.00[b]
468.9	0.0994	0.0079	0.2061	147.8	27.89	0.8422	30.41	26.9[a]
468	0.1	0	0	148.0	27.91	0.8420	40.52	27.0[a]
543	0.1987	0.0158	0.2278	242.1	34.59	0.8011	65.51	33.0[a]
501.6	0.2484	0.0198	0.2508	250	35.37	0.7874	74.14	
3714	0.01	0	0	371.4	38.27	0.8592	24.03	38.03[c]
3714	0.01	0.005	0.2594	371.4	38.28	0.8590	24.03	38.13[d]
3714	0.01	0.01	0.5188	371.4	38.30	0.8586	24.08	
1295	0.0975	0.0155	0.2468	404.4	40.81	0.8173	75.87	39.0[a]
1003	0.2484	0.0198	0.1774	500	46.53	0.7579	140.9	
3957	0.025	0	0	625.6	47.44	0.8379	61.67	48.27[e]
1648	0.1951	0.031	0.2602	727.8	53.95	0.7744	182.8	51.8[a]
2500	0.1104	0	0	830.6	55.14	0.8015	162.0	56.69[a]
2006	0.2484	0.0198	0.1254	1000	62.56	0.7519	274.1	
3034	0.1104	0	0	1008	59.98	0.8019	195.3	62.58[e]
4000	0.25	0.02	0.0894	2000	85.85	0.7459	536.2	
10000	0.25	0.02	0.0566	5000	130.7	0.7377	1260	

TABLE 2. Effect of the Dean number under small torsion. The sources of fRe_{Lit} are [a] Manlapaz & Churchill (1980); [b] Truesdell & Adler (1970); [c] Dennis & Ng (1982) for $\lambda = 0$, $\eta = 0$; [d] Yang & Keller (1986) for $\lambda = 0$, $\eta = 0$; [e] Austin & Seader (1973). The asterisk denotes both the decimal point and the number listed being 100γ*

to that shown in table 1. In all the cases, the flow patterns are very similar indicating once again that as long as the loose coiling approximation is met and $\gamma \leqslant 0.01$, the flow corresponds to a torus-like flow.

4.2. *Effect of the Dean number on helical flows for a fixed pipe geometry*

To proceed with the examination of the effect of the Dean number on the helical flow, the solution properties for selected small-torsion helical pipes with various Dean numbers and helical geometries are shown in table 2. $\Delta p_{max} = p_{max} - p_{min}$ is the maximum pressure difference across the pipe. For comparison, some friction factor values from the literature are listed and denoted by fRe_{Lit}.

In the limit of zero pitch, $\eta = 0$, i.e. for toroidal flow, one calculation was made with the same conditions as those of Truesdell & Adler (1970) at $Dn = 122.9$, $\lambda = 0.01$, $\eta = 0$. The agreement between our result and theirs is relatively good, with a deviation of about 2%. More comparisons were made with the studies of Austin & Seader (1973) and Manlapaz & Churchill (1980). It is found that at small Dn, the results are in better agreement with these investigators' results. However, for large Dn ,the results of Austin & Seader are on the higher side and the results of Manlapaz & Churchill are on the lower side. To compare with the more accepted fRe values, we calculated the case of

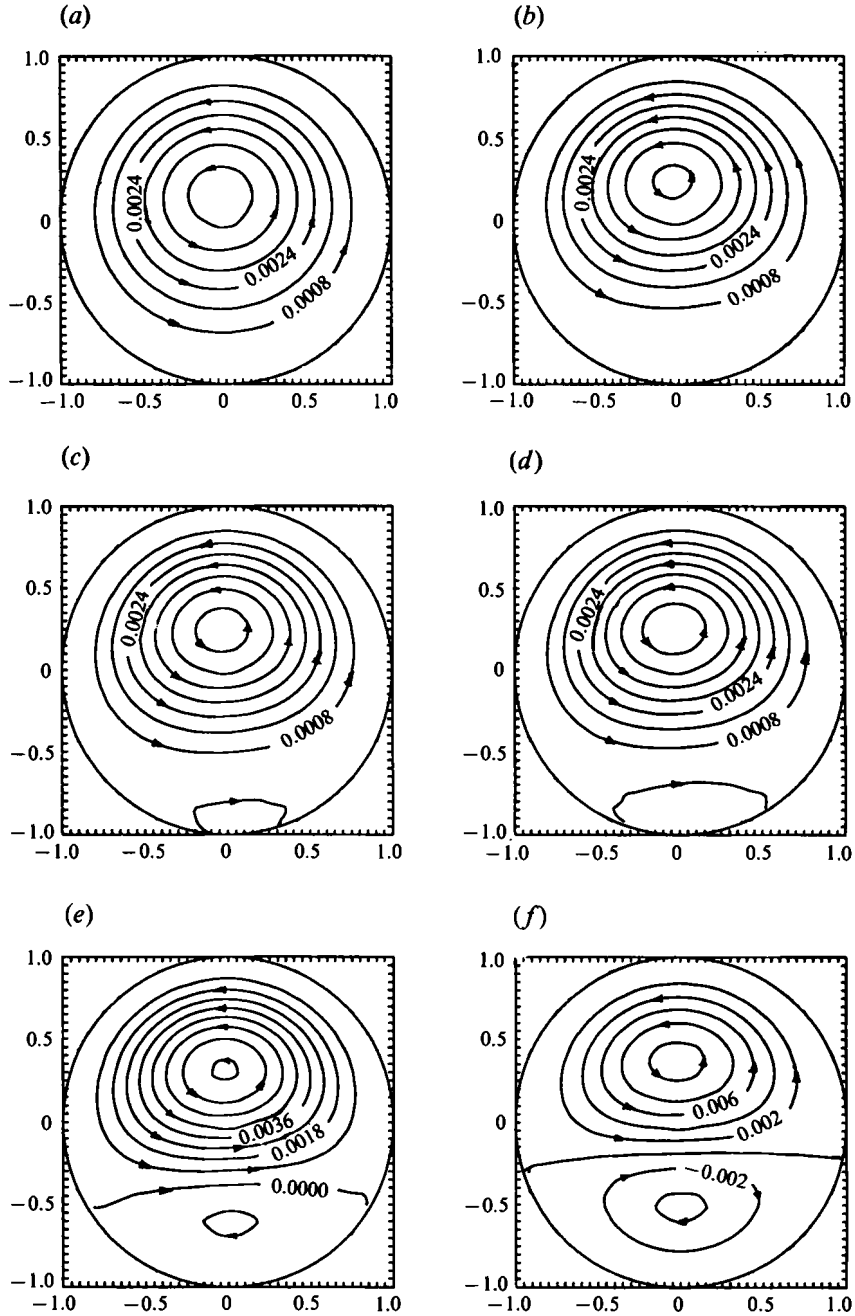

FIGURE 3. Dean number effect on secondary flow patterns for a fixed helical pipe geometry of R_c = 4, $H = 2$, $Dn \leqslant 4$. (*a*) $Dn = 0.5$, $\gamma^* = 0.07933$; (*b*) $Dn = 1.0$, $\gamma^* = 0.03966$; (*c*) $Dn = 1.1$, $\gamma^* = 0.03606$; (*d*) $Dn = 1.2$, $\gamma^* = 0.03305$; (*e*) $Dn = 2.0$, $\gamma^* = 0.01983$; (*f*) $Dn = 4.0$, $\gamma^* = 0.009916$.

$Dn = 371.4$, $\lambda = 0.01$, $\eta = 0$ to simulate the loose coiling solution of Dennis & Ng (1982) and Yang & Keller (1986). It is found that the fRe value is in very good agreement with the work of Dennis & Ng (1982), with a deviation less than 0.7% and that of Yang & Keller (1986), with a deviation of less than 0.4%.

Manlapaz & Churchill (1980) also studied steady laminar flow in a helical pipe with a small pitch, $H \leqslant R_c$, but their solution used a non-orthogonal coordinate system and

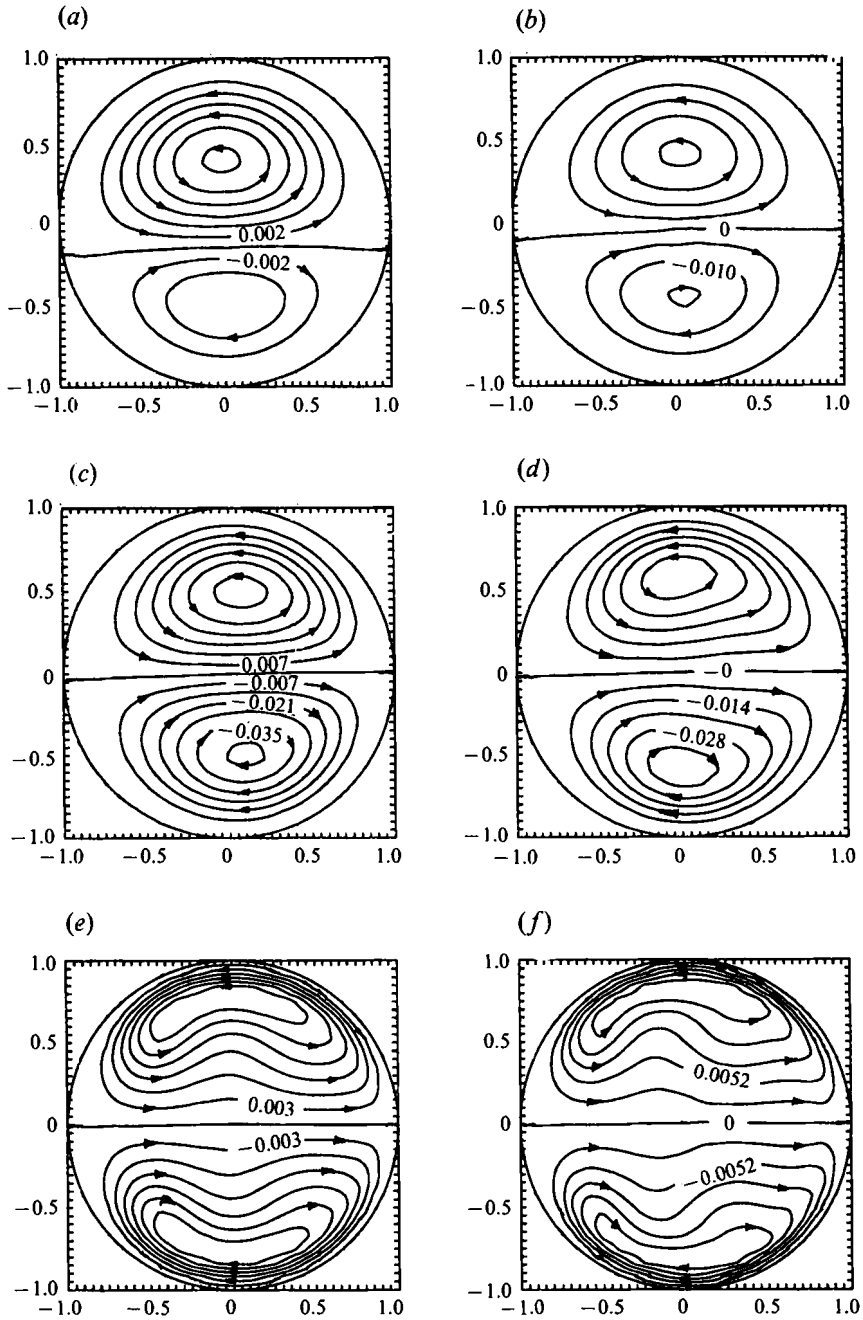

FIGURE 4. Dean number effect on secondary flow patterns for a fixed helical pipe geometry of R_c = 4 and $H = 2$. (*a*) $Dn = 5$, $\gamma = 0.01774$; (*b*) $Dn = 10$, $\gamma = 0.01254$; (*c*) $Dn = 50$, $\gamma = 0.005609$; (*d*) $Dn = 100$, $\gamma = 0.003966$; (*e*) $Dn = 500$, $\gamma = 0.001774$; (*f*) $Dn = 1000$, $\gamma = 0.001254$.

their helical flow problems have a γ of less than 0.015 for $Dn > 20$. The deviation for fRe values is up to 5%. The higher deviation from Manlapaz & Churchill's results at higher Dn could be due to their extrapolation which was based on the solutions for too coarse grid sizes.

For very small Dean number flows, the current calculations in table 2 show the same behaviour as that of the toroidal flow findings in the literature (see Manlapaz &

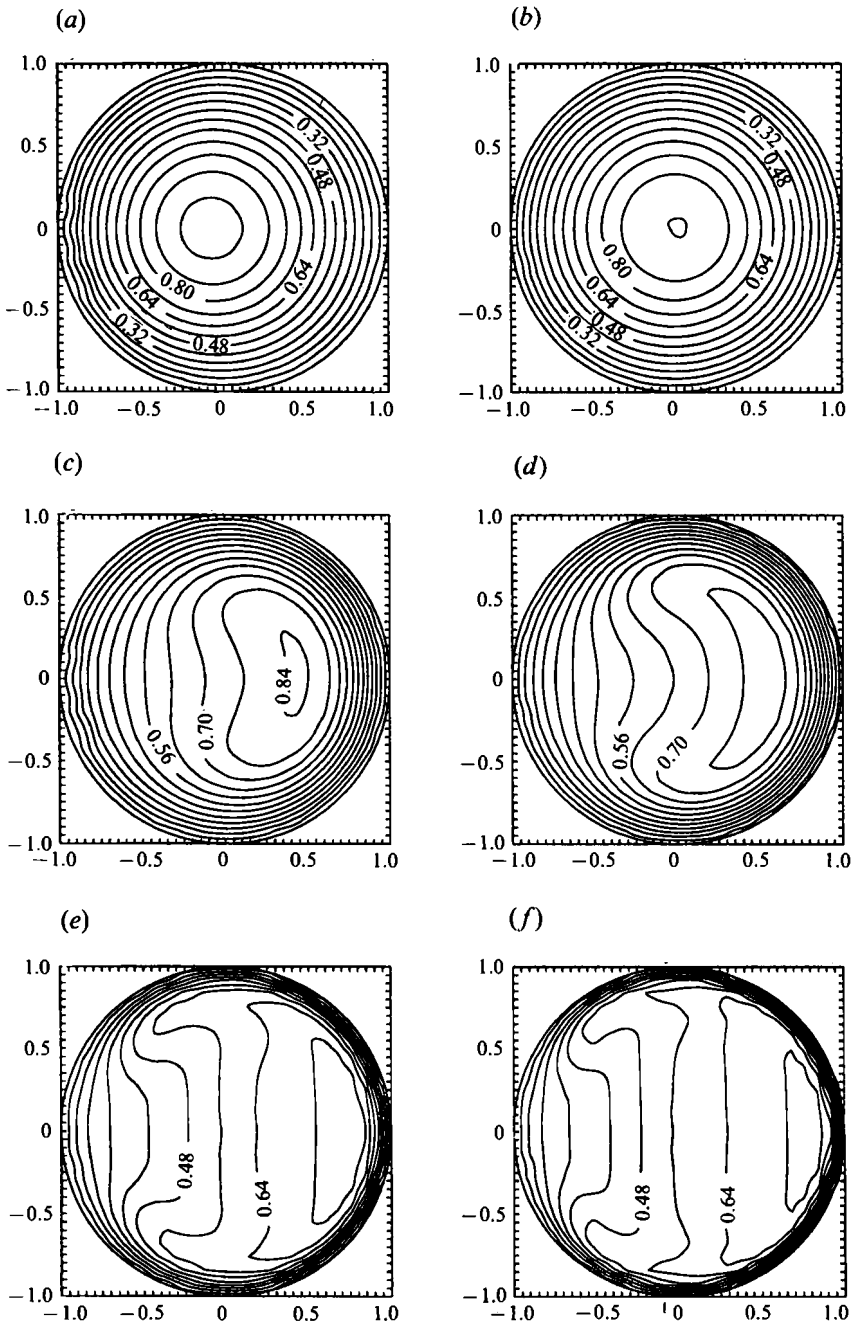

FIGURE 5. Dean number effect on axial velocity profiles for a fixed helical pipe geometry of $R_c = 4$ and $H = 2$. (*a–f*) Dn and γ values as for figure 4.

Churchill 1980). When $Dn < 20$, the friction factor exhibits a very small dependence on Dn. The friction factor can be smaller than its counterpart in straight pipe flow for $Re \ll 1$ (Chadwick 1985; Van Dyke 1990).

In §3, the influence of relative torsion or Gn on the helical pipe flow at very small Dean numbers was shown to be governed by γ^*. Figure 3 shows the secondary flow patterns for a fixed helical pipe of $R_c = 4$ and $H = 2$ with $Dn \leqslant 4$. As would be

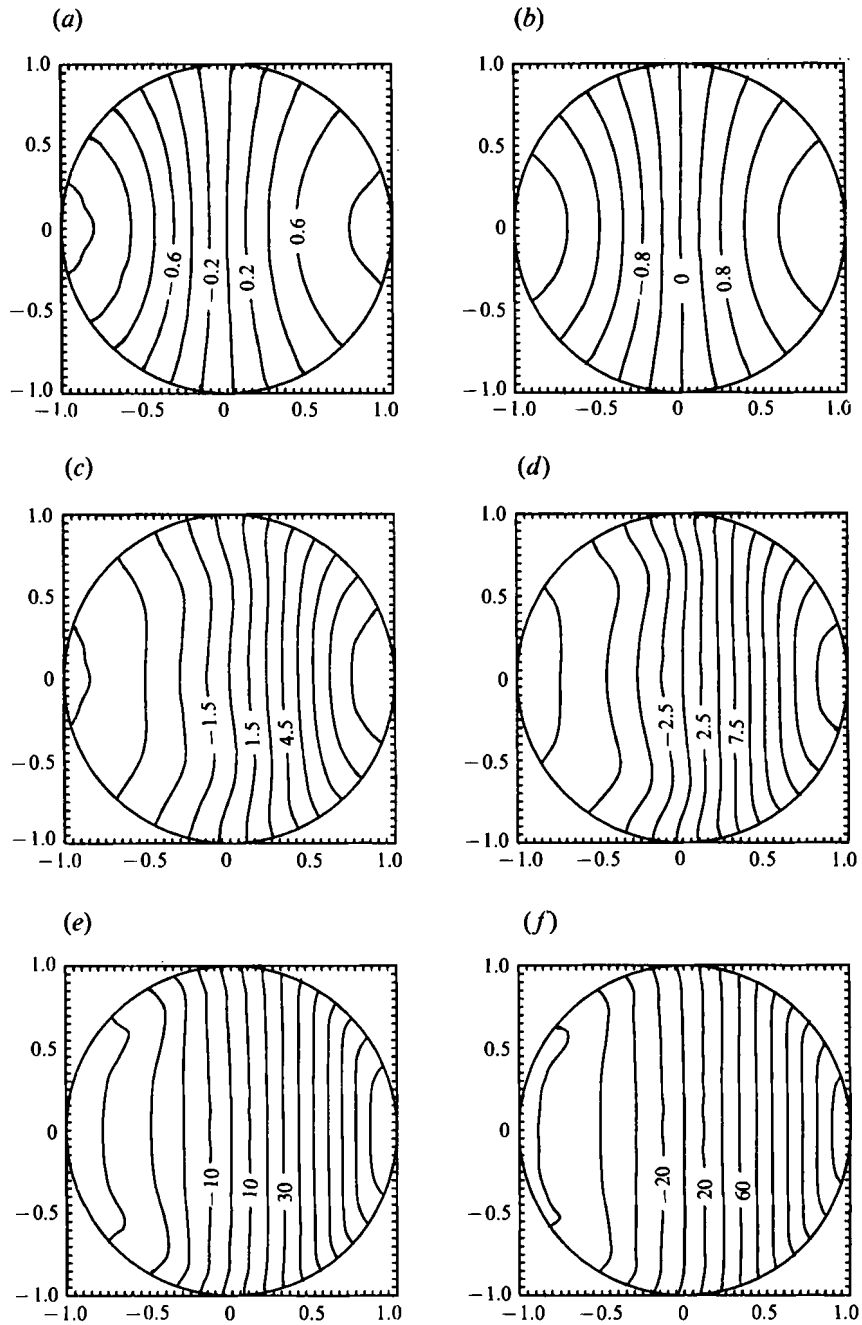

FIGURE 6. Dean number effect on pressure contours for a fixed helical pipe geometry of $R_c = 4$ and $H = 2$. (*a–f*) Dn and γ values as for figure 4.

expected, the flow is swirl-like. As Dn increases, an additional vortex appears from the bottom of the pipe. The size and the strength of the second vortex increase as Dn increases.

Figures 4–6 show the effect of the Dean number on the helical flow behaviour for the same geometry as that of figure 3 for $Dn \geqslant 5$. As an extension of figure 3, figure 4 shows that the lower vortex expands until it is equivalent to the upper vortex, at which the

H	$10^{-4}\,Re$	λ	η	γ	fRe	u_{max}	Δp_{max}	ψ_{max}	$-\psi_{min}$
0	0.06	0.11111	0	0	31.24	0.8341	42.42	0.02152	0.02152
10	0.06093	0.10774	0.01905	0.0041	31.21	0.8351	41.87	0.02135	0.02092
20	0.06364	0.09876	0.03493	0.0079	31.14	0.8380	40.30	0.02062	0.01981
40	0.07349	0.07406	0.05238	0.0136	30.93	0.8452	35.48	0.01826	0.01689
18π	0.08485	0.05556	0.05556	0.0167	30.76	0.8508	31.12	0.01605	0.01454
100	0.1219	0.02692	0.04761	0.0205	30.46	0.8595	22.13	0.01143	0.01004
200	0.2205	0.008225	0.02909	0.0227	30.25	0.8654	12.41	0.006403	0.005521
900	0.9568	4.369×10^{-4}	6.954×10^{-3}	0.0235	30.16	0.8679	2.879	0.001484	0.001270
10^4	10.6104	3.553×10^{-6}	6.283×10^{-4}	0.0236	30.15	0.8680	0.2597	1.34×10^{-4}	1.14×10^{-4}
10^6	1061.04	3.55×10^{-10}	6.283×10^{-6}	0.0236	30.15	0.8680	0.0026	1.34×10^{-6}	1.14×10^{-6}

TABLE 3. Effect of torsion on helical flows with $R_c = 9$, $Dn = 200$

R_c	$10^{-4}\,Re$	λ	$10^6\eta$	γ	fRe	u_{max}	Δp_{max}	ψ_{max}	$-\psi_{min}$
1	636.6	3.95×10^{-11}	6.283	0.05	41.44	0.4645	0.0019	4.521×10^{-7}	2.871×10^{-7}
2	450.1	7.90×10^{-11}	6.283	0.0354	40.50	0.5122	0.0025	5.209×10^{-7}	3.995×10^{-7}
5	284.7	1.97×10^{-10}	6.283	0.0224	39.75	0.5391	0.0038	7.545×10^{-7}	6.439×10^{-7}
10	201.3	3.95×10^{-10}	6.283	0.0158	39.50	0.5476	0.0052	1.041×10^{-6}	9.266×10^{-7}
40	100.6	1.579×10^{-9}	6.283	0.0079	39.30	0.5537	0.0103	2.037×10^{-6}	1.922×10^{-6}
100	63.66	3.948×10^{-9}	6.283	0.005	39.25	0.5549	0.0163	3.203×10^{-6}	3.084×10^{-6}
10^3	20.13	3.948×10^{-8}	6.283	0.0016	39.23	0.5556	0.0515	1.006×10^{-5}	9.945×10^{-6}
10^4	6.379	3.932×10^{-7}	6.258	0.0005	39.23	0.5557	0.1623	3.170×10^{-5}	3.159×10^{-5}
10^6	4.050	9.753×10^{-7}	0.1552	8×10^{-6}	39.23	0.5557	0.2557	4.989×10^{-5}	4.989×10^{-5}

TABLE 4. The effect of torsion on helical flows for $H = 10^6$, $Dn = 400$

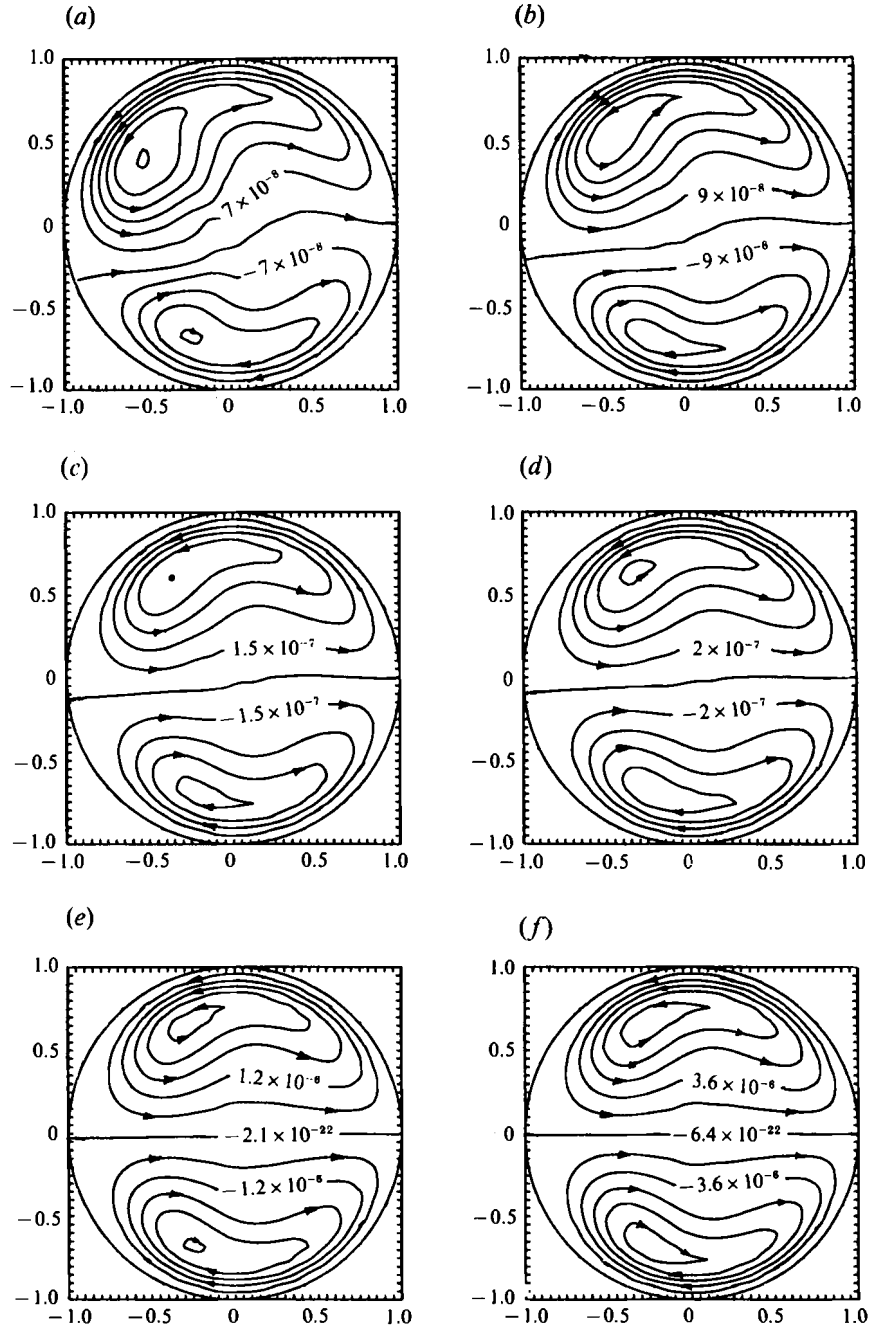

FIGURE 7. Secondary flow patterns for $Dn = 400$, $H = 10^6$ and $\eta \approx 6.28 \times 10^{-6}$ with varying R_c. (*a*) $R_c = 1$, $\gamma = 0.05$; (*b*) $R_c = 2$, $\gamma = 0.0354$; (*c*) $R_c = 5$, $\gamma = 0.0224$; (*d*) $R_c = 10$, $\gamma = 0.0158$; (*e*) $R_c = 100$, $\gamma = 0.005$; (*f*) $R_c = 1000$, $\gamma = 0.0016$.

flow becomes torus-like with two vortices of equal size and strength but opposite direction of rotation. With *Dn* increasing, the secondary flow streamlines (tubes) become denser near the wall and sparser in the centre region. The two vortices always appear to be up-and-down. The location of the maximum axial velocity, shown in figure 5, moves away from the centre of the pipe toward the outer wall as the Dean

number increases, and the centre region is flat. As Dn increases, the flat area expands to form a larger 'plateau'. The plateau is inclined with the outer region having a higher value than the inner region. The value of the pressure away from the centre, which is set to zero, increases as the Dean number becomes larger. When Dean number is large, as shown in figure 6, the pressure varies sharply in the y-direction and its variation in the x-direction is negligible. When Dn is small, the pressure isobar lines are also vertically oriented but bent towards either the inner or the outer wall.

4.3. *Effect of pitch on helical flows for a fixed Dn and* R_c

To investigate the Germano number effect on the flow in a helical pipe, we computed the solutions for a family of helical pipes with the same radius of coil, $R_c = 9$. Table 3 shows the results for $Dn = 200$ and $R_c = 9$, indicating that as H increases, the values of fRe and u_{max} become invariant with H. Also $Re\,\Delta p_{max}$ (or $\lambda^{-\frac{1}{2}}\Delta p_{max}$), $Re\,\psi_{max}$ and $Re\,\psi_{min}$ (or $\lambda^{-\frac{1}{2}}\psi_{max}$ and $\lambda^{-\frac{1}{2}}\psi_{min}$) become independent of H. An explanation for such behaviour is given below.

The limit of large H corresponds to the range where Gn becomes constant. When the pitch is large, the torsion and the curvature ratio satisfy the relationship

$$\lambda = R_c\,\eta^2. \tag{41}$$

Consequently,

$$Gn = Dn/R_c^{\frac{1}{2}} \quad (H \to \infty). \tag{42}$$

The above relationship indicates that in the limit of large H, $\lambda \to 0$ as $\eta \to 0$ and Gn becomes a constant for given R_c and Dn. For loosely coiled pipes, the flow is dependent only on Dn and Gn. Hence, it is expected that the flow behaviour will be invariant as $H \to \infty$. Indeed, the two bottom rows of table 3 show that fRe and u_{max} become identical as H is increases.

4.4. *The effect of* R_c *on helical flows at a fixed Dn and large H*

In §4.3, we examined the effect of pitch and the loose coiling limit by varying the pitch. Here, we examine the loose-coiling limit by varying the radius of the coil, R_c, for large H. As was indicated in the section on the loose-coiling analysis, the flow behaviour should become that of a loosely coiled pipe of negligible torsion (γ is very small), i.e. Dean flow, as the radius of the coil is increased. Table 4 shows the results for this case. It can be seen that at small R_c, $|\psi_{max}|$ and $|\psi_{min}|$ are very different. As R_c increases, the difference between $|\psi_{max}|$ and $|\psi_{min}|$ decreases. All the flow characteristics tend to be invariant as R_c becomes very large. Once again, the scaling of ψ and Δp_{max} has been taken into account to arrive at the above conclusion.

Secondary flow patterns are shown in figure 7 for $Dn = 400$, $H = 10^6$: it can be seen that although the pitch of the helical coils is very large, the flow behaviour is close to the loosely coiled helical flow of negligible torsion effect for $R_c > 10$. With the help of table 4, we may conclude that the torsion effect is negligible when $R_c \geqslant 40$. Hence, it is not necessary to require a coil radius greater than the pitch for the flow in a helical pipe to be torus-like.

4.5. *The effect of torsion and flow pattern transition*

From the definition of γ as given by (38), if Dn and λ are constant, γ can only change through the variation of the torsion η. Consequently, γ and η become linearly related to each other and hence one can refer to γ or η interchangeably. When Dn is fixed, the centrifugal forces are kept constant. As the torsion increases, the increase in the 'twisting' forces results in a higher secondary flow strength. Hence, although Dn and λ are kept constant, the secondary flow strength is still expected to rise as γ (or η) increases. When η (or γ) is large, the body-centred azimuthal velocity $\xi = w - \eta r u/h_1$

η	γ	fRe	$u_{0,0}$	u_{max}	p_{max}	$-p_{min}$	ψ_{max}	$-\psi_{min}$
$Dn = 20$, $Re = 80$, $\lambda = 0.0625$								
0	0	16.80	0.9300	0.9835	2.565	1.506	0.0166	0.0166
0.1875	0.1677	16.76	0.9382	0.9879	2.460	1.607	0.04462	0.000315
0.24206	0.2164	16.72	0.9443	0.9916	2.366	1.666	0.05488	0
1	0.8944	16.12	0.9985	1.002	1.117	1.248	0.2460	0
$Dn = 50$, $Re = 200$, $\lambda = 0.0625$								
0	0	20.29	0.7324	0.9024	6.977	2.465	0.02307	0.02307
0.35355	0.2	19.75	0.7995	0.9601	6.266	2.344	0.04978	0.00193
0.44194	0.25	17.96	0.9206	1.001	4.103	3.283	0.08332	0
1.4142	0.8	16.17	0.9986	1.000	1.471	1.635	0.3844	0
$Dn = 100$, $Re = 2000$, $\lambda = 0.0025$								
0	0	23.80	0.6313	0.8779	2.697	0.821	0.004133	0.004133
0.09	0.18	19.73	0.8706	0.9747	1.874	0.759	0.01289	0.00011
0.11	0.22	17.89	0.9499	0.9802	1.429	1.076	0.02118	0
0.5	1	16.08	0.9944	0.9946	0.7928	0.7899	0.1224	0
$Dn = 100$, $Re = 1000$, $\lambda = 0.01$								
0.02	0.02	23.94	0.6288	0.8733	5.406	1.648	0.008771	0.007658
0.185	0.185	19.54	0.8929	0.9796	3.476	1.653	0.02808	0.0002
0.2	0.2	18.73	0.9290	0.9812	3.066	1.925	0.03461	0
1	1	16.07	0.9975	0.9977	1.127	1.154	0.2463	0
$Dn = 100$, $Re = 400$, $\lambda = 0.0625$								
0	0	24.26	0.6343	0.8571	12.67	4.40	0.02045	0.02045
0.45	0.18	20.98	0.8937	0.9968	8.077	3.812	0.06109	0.0005
0.625	0.25	18.18	0.9715	0.9920	5.238	5.036	0.1327	0
1	0.4	16.86	0.9855	0.9903	3.525	3.845	0.2383	0
$Dn = 100$, $Re = 250$, $\lambda = 0.16$								
0	0	24.95	0.6374	0.8260	18.40	7.88	0.03210	0.03210
0.8	0.2	21.13	0.9589	1.022	8.441	7.016	0.1470	0.0001
0.9	0.225	19.99	0.9742	1.011	7.134	7.110	0.1826	0
1.2	0.3	18.22	0.9818	0.9954	5.026	5.995	0.2784	0

TABLE 5. Effect of torsion on helical flows

is dominated by the twisting component $\eta ru/h_1$. Since the axial velocity u is expected to be sign-conservative (irrespective to the change of θ), it follows that the secondary flow is expected to be uni-directional, i.e. one-vortex or swirl-like at large η values.

Table 5 gives a summary of the numerical simulation results for the torsion effect on the small to moderate Dn flows for selected cases. In each case, Dn and λ are fixed and only γ, or the torsion η, varies. From table 5, we observe that the pressure difference decreases as γ increases. The cross-plane pressure difference decrease suggests that the secondary flow strength due to the centrifugal forces decreases. A limit of non-zero value is expected for the secondary flow strength due to the fixed centrifugal forces from the governing equations (17) and (18). The value of this limit is, however, insignificant compared to the secondary flow strength due to the 'twisting' forces. It is then expected that the centre and the maximum axial velocities increase and the main flow becomes close to a straight-pipe Poiseuille-like flow as the centrifugal force effects become insignificant. On the other hand, the secondary flow strength in the non-orthogonal coordinate system, $\psi_{max} - \psi_{min}$, which includes the effect of the rotation of the pipe geometry, increases proportionally with γ. Hence, the overall non-orthogonal secondary flow strength, $\psi_{max} - \psi_{min}$, due to the twisting forces increases more rapidly than its decrease due to the centrifugal forces.

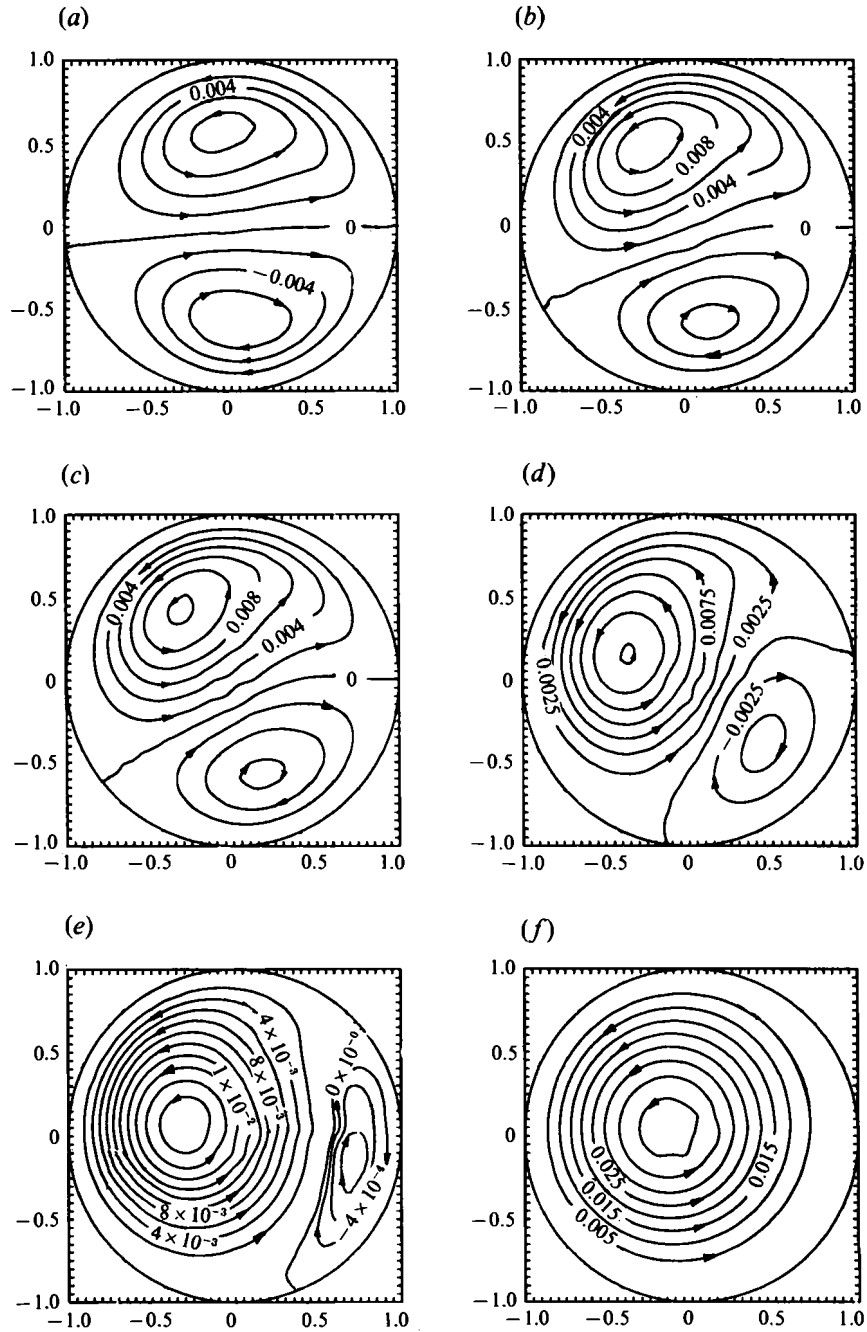

FIGURE 8. Secondary flow patterns for $Re = 1000$, $Dn = 100$, $\lambda = 0.01$ and $\gamma > 0.01$. All the contour lines are equally spaced except in (*e*), where the small vortex on the left is exactly one order of magnitude smaller in scaling. (*a*) $\gamma = \eta = 0.02$; (*b*) $\gamma = \eta = 0.08$; (*c*) $\gamma = \eta = 0.0995$; (*d*) $\gamma = \eta = 0.15$; (*e*) $\gamma = \eta = 0.17$; (*f*) $\gamma = \eta = 0.22$.

When $\gamma > 0.2$, the minimum pseudo-secondary flow stream function value increases to zero. This marks the elimination of one vortex which is represented by the negative value of the pseudo-secondary flow stream function. Although Dn and λ vary over a wide range as shown in table 5, the transition point is given by $\gamma \approx 0.2$. Hence, the

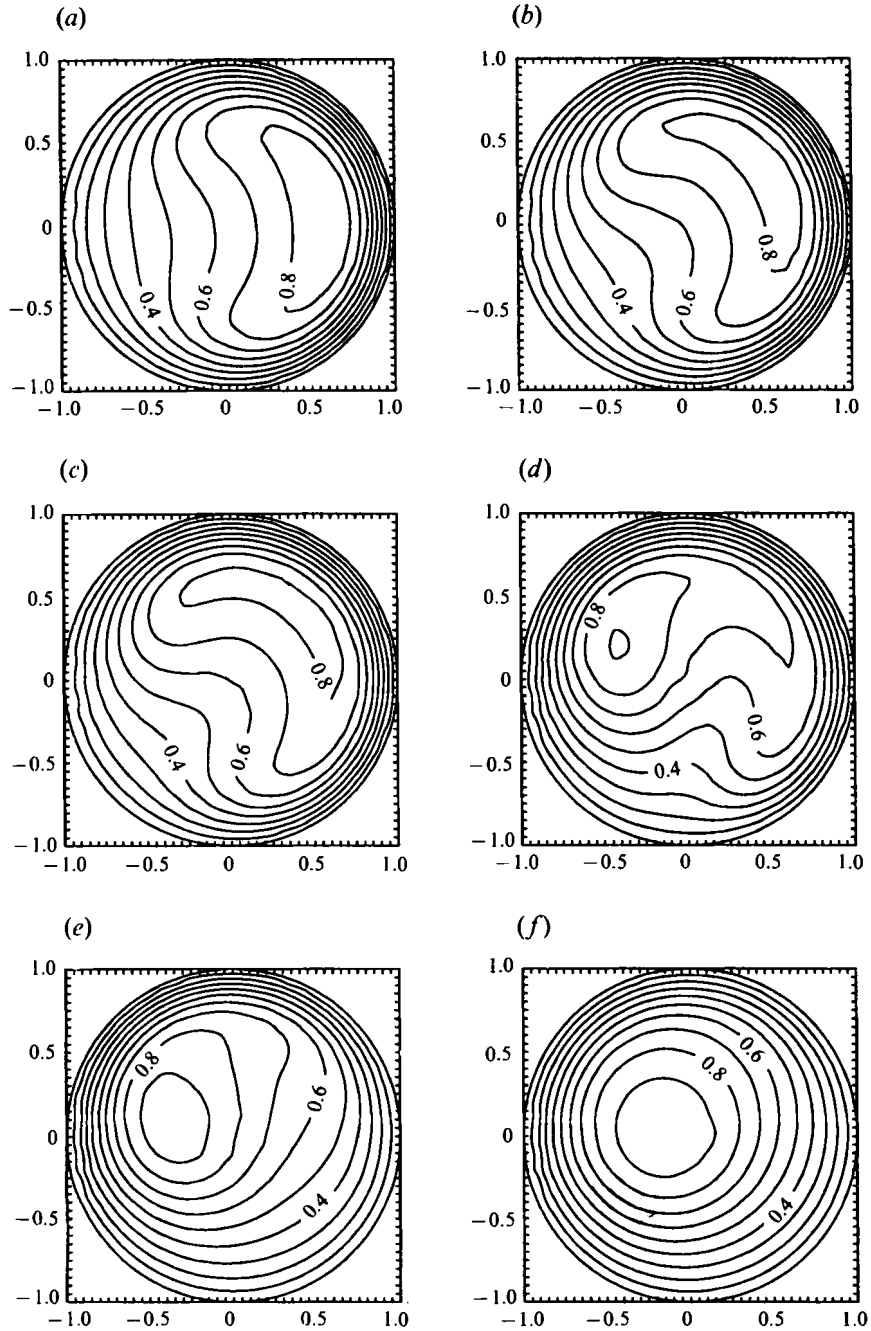

FIGURE 9. Iso-axial velocity contours for $Re = 1000$, $Dn = 100$, $\lambda = 0.01$ and $\gamma > 0.01$. (*a–f*) γ and η values same as figure 8.

transition from two-vortex to one-vortex flow for large-Dn systems is characterized by γ.

To show the flow transitions and other characteristics, some contour plots and the axial wall shear rate $(-\partial u/\partial r|_{r=1})$ are shown in figures 8–11 for $Dn = 100$, $\lambda = 0.01$.

Figure 8 shows that the secondary flow pattern varies from an almost symmetric two-vortex torus-like pattern to a single-vortex swirl-like pattern as γ is increased. On

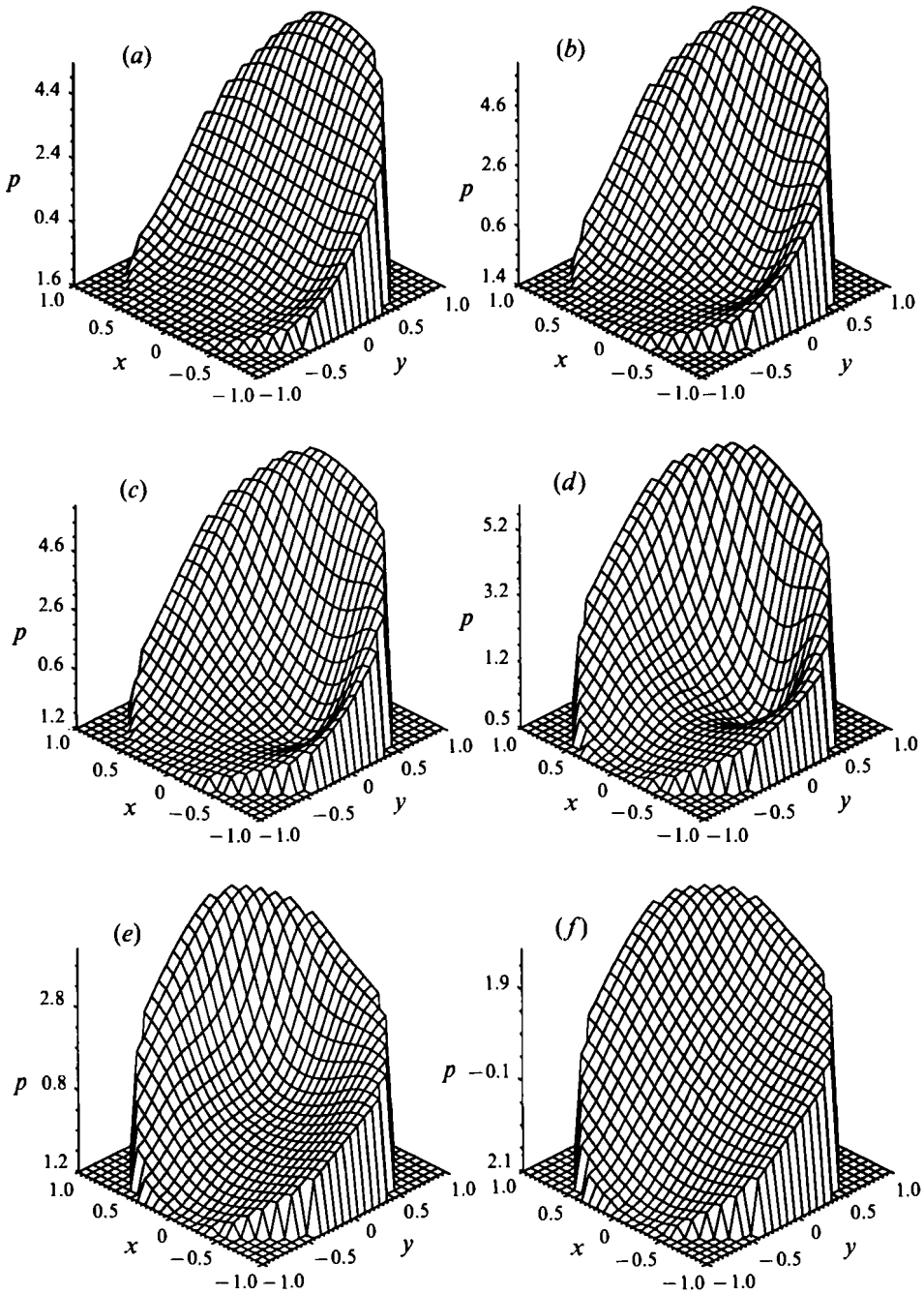

FIGURE 10. Pressure profiles for $Re = 1000$, $Dn = 100$, $\lambda = 0.01$ and $\gamma > 0.01$. (*a–f*) γ and η values same as figure 8.

increasing γ, the upper vortex increases both in strength and in size while the lower vortex becomes weaker. The bending of the dividing line between the two vortices can be observed as γ increases and it is viewed as the distortion generated by the torsion of the helical pipe. The distortion is more evident at larger Dn. The pattern becomes that of two vortices turning anticlockwise as the lower vortex (negatively ψ-valued vortex) loses both its strength and its size. However, on approaching the disappearance

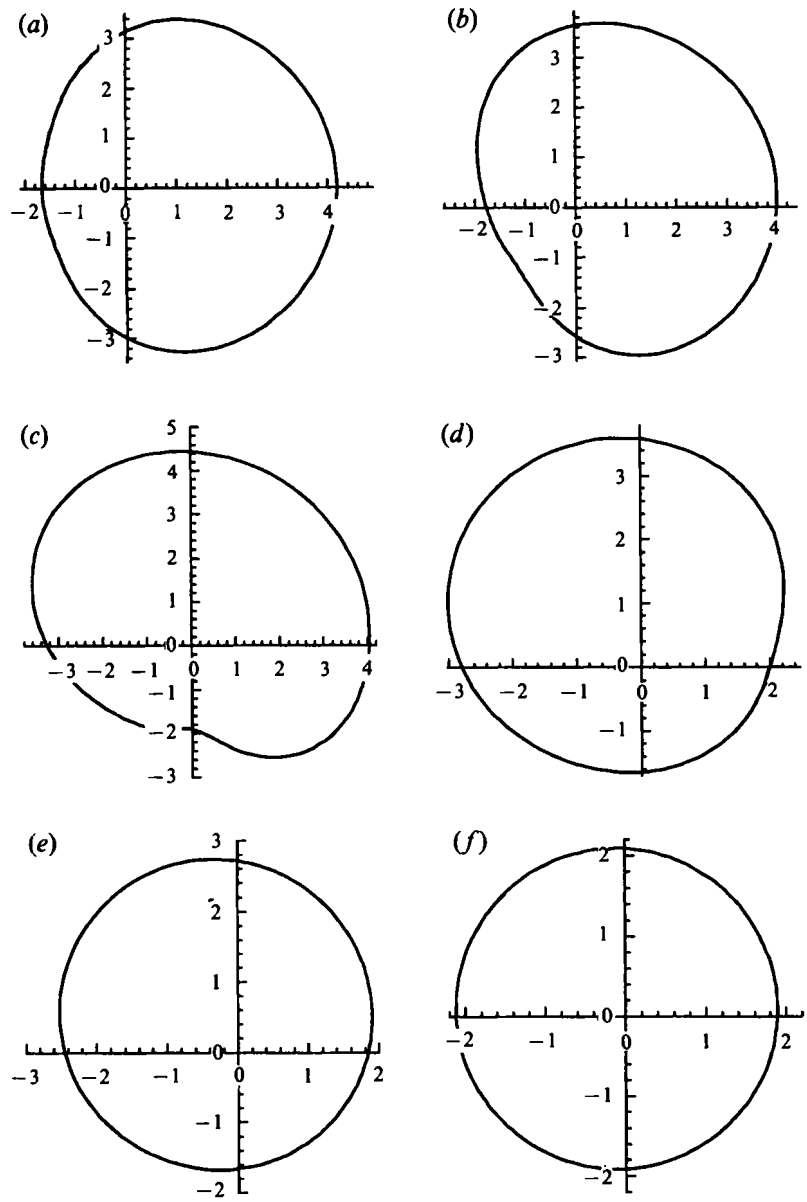

FIGURE 11. Axial wall shear rate distribution across the pipe wall circumference for $Dn = 100$, $\lambda = 0.01$ and various γ. The value of the axial wall shear rate is the polar distance from the origin of each plot (0,0). (*a*) $\gamma = 0.01$, (*b*) $\gamma = 0.08$, (*c*) $\gamma = 0.15$, (*d*) $\gamma = 0.17$, (*e*) $\gamma = 0.22$, (*f*) $\gamma = 1.0$.

of the negatively ψ-valued vortex, its size reduces rather slowly while its strength reduces much faster. For large-*Dn* flow, as shown in figure 8, two vortices appear to be left and right, or inner and outer. The lower or right (outer) vortex eventually disappears as $\gamma > 0.2$. Figure 8 and table 5 indicate that the flow pattern transition from a two- to one-vortex pattern occurs at $\gamma \simeq 0.2$.

The axial velocity isopleths, shown in figure 9, rotate anticlockwise with the maximum axial velocity location moving slowly towards the centre of the pipe as the torsion increases. At large γ, the axial velocity approaches that of the axisymmetrical straight-pipe Poiseuille-like axial velocity.

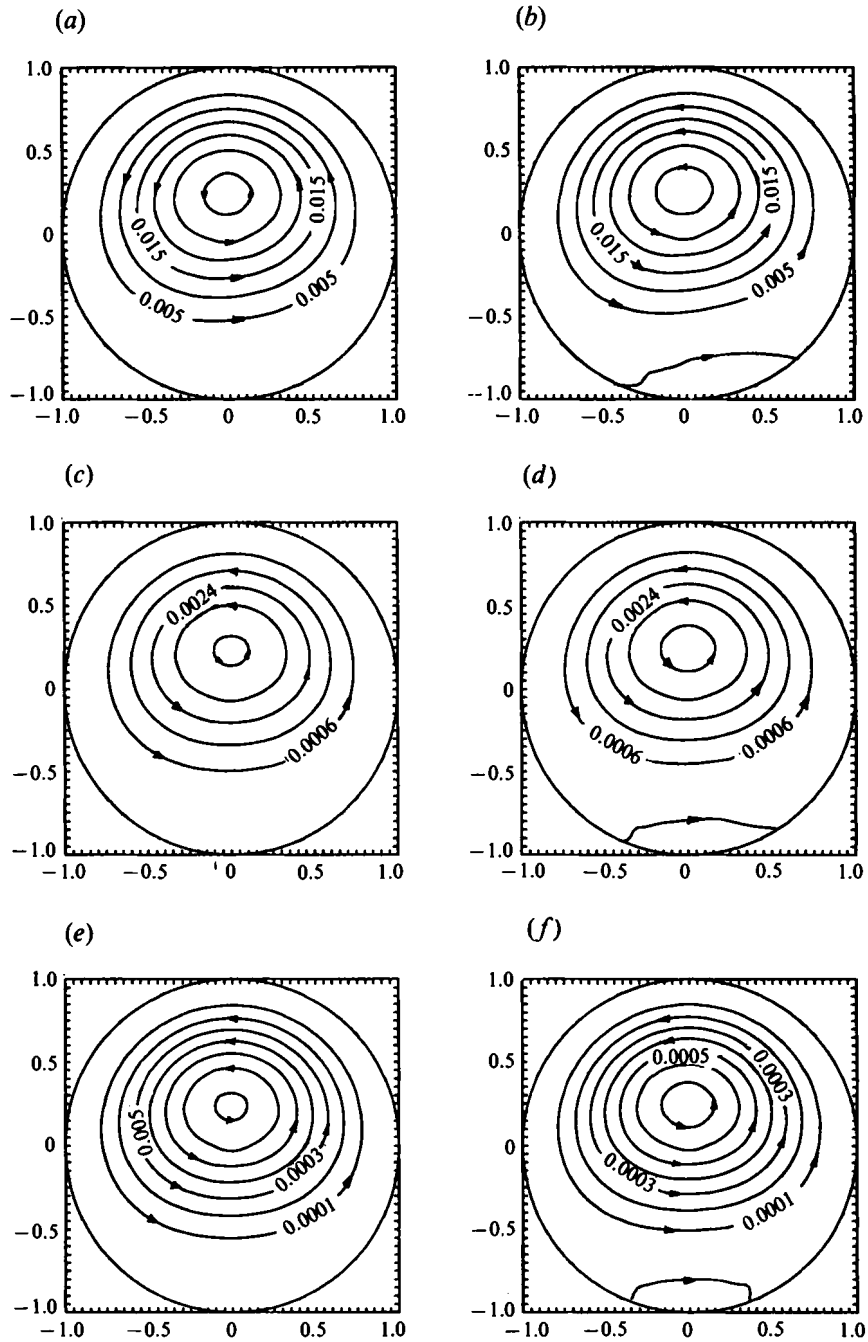

FIGURE 12. Transition from two-vortex to one-vortex flow for $Dn < 20$. (*a*) $Dn = 10.2$, $\gamma^* = 0.0415$, $\gamma = 0.01299$; (*b*) $Dn = 11.74$, $\gamma^* = 0.03606$, $\gamma = 0.01052$; (*c*) $Dn = 5.14$, $\gamma^* = 0.0415$, $\gamma = 0.0183$; (*d*) $Dn = 5.916$, $\gamma^* = 0.03606$, $\gamma = 0.01482$; (*e*) $Dn = 0.2395$, $\gamma^* = 0.0415$, $\gamma = 0.0848$; (*f*) $Dn = 0.2756$, $\gamma^* = 0.03606$, $\gamma = 0.06869$.

A surface plot of the pressure is shown in figure 10 for $Dn = 100$ and $\lambda = 0.01$. The surface of the pressure profile becomes less smooth, even with a locally low-pressure zone (cone) forming in helical pipes of large torsion near the lower wall as γ increases. Figure 10(*d*) shows clearly a low-pressure cone. Here, $\gamma = 0.15$ and the hole (minimum

λ	η	Gn	γ	fRe	$u_{0,0}$	u_{max}	p_{max}	$-p_{min}$
$Dn = 20$								
0.0001	0	0	0	16.61	0.9291	0.9953	0.1091	0.0564
0.2	0	0	0	17.17	0.9293	0.9598	4.019	3.120
0.5	0	0	0	17.86	0.9094	0.9126	4.802	6.885
0.8	0	0	0	18.46	0.8657	0.8691	4.581	13.30
$Dn = 100$								
0.04	0	0	0	24.12	0.6321	0.8649	10.35	3.45
0.2	0	0	0	25.21	0.6383	0.8144	19.81	9.22
0.2	0.1	22.36	0.0224	25.36	0.6374	0.8120	20.11	9.07
0.2	0.2	44.72	0.0447	25.78	0.6349	0.8045	20.94	8.61
0.5	0	0	0	26.89	0.6363	0.7484	23.90	20.84
0.5	0.25	35.36	0.0354	27.83	0.6464	0.7611	25.32	19.61
0.5	0.5	70.71	0.0707	30.40	0.6680	0.7692	29.13	15.58
1	0	0	0	28.26	0.6156	0.8442	29.13	97.96
$Dn = 500$								
0.0001	0	0	0	42.90	0.5553	0.8554	2.547	0.649
0.2	0	111.8	0	46.20	0.5756	0.7775	92.72	36.12
0.2	0.1	111.8	0.01	46.60	0.5739	0.7748	94.39	35.54
0.2	0.2	223.6	0.02	47.80	0.5683	0.7672	99.19	33.59
0.5	0	0	0	49.82	0.5926	0.6900	112.0	81.2
0.5	0.25	176.8	0.0158	52.07	0.5997	0.6907	118.8	76.2
0.5	0.5	353.6	0.0316	58.65	0.6111	0.6909	138.2	59.1
1	0	0	0	51.77	0.5670	0.6968	102.3	394.1

TABLE 6. The effect of the curvature ratio under small torsion

pressure zone) is located near the lower wall. This pressure cone is again attributed to the distortion effect of the torsion.

The variation of the axial wall shear rate distribution along the pipe wall circumference with torsion is shown in figure 11. It can be observed that the axial wall shear rate is higher near the outer wall when γ is small. As γ increases, the location of the maximum axial wall shear rate moves towards the inner upper wall. When γ is large, the axial wall shear rates becomes almost uniformly distributed as shown in figure 11(f).

Figure 12 shows the validity of γ^* as the flow transition parameter for $Dn < 20$. It can be seen that changes in Dn and γ or Re do not reflect the flow pattern transition. However, the secondary flow pattern has two vortices at $\gamma^* = 0.03606$ and one vortex at $\gamma^* = 0.0415$. The critical value is $\gamma^* = 0.039$. Note that Wang (1981) found the same group ($\eta/\lambda\, Re = \frac{1}{24} = 0.0417$) from his perturbation series solution. The currently determined critical value of γ^* is slightly smaller than that of Wang by about 7%.

4.6. *The effect of the curvature ratio*

The effect of the curvature ratio λ on the helical flow has not been investigated in great detail in the past. Some results are listed in table 6.

Contours showing the secondary flow patterns with various λ for toroidal flows of $Dn = 500$ are presented in figure 13. It can be concluded from figure 13 that the secondary flow patterns look remarkably similar, even though λ changes from 0.04 to an extremely tight torus. For small λ, the two vortices are almost equally separated near the inner wall and near the outer wall. However, for λ approaching unity, the two vortices are farther apart near the inner wall, where the secondary flow is weaker than that at the outer wall.

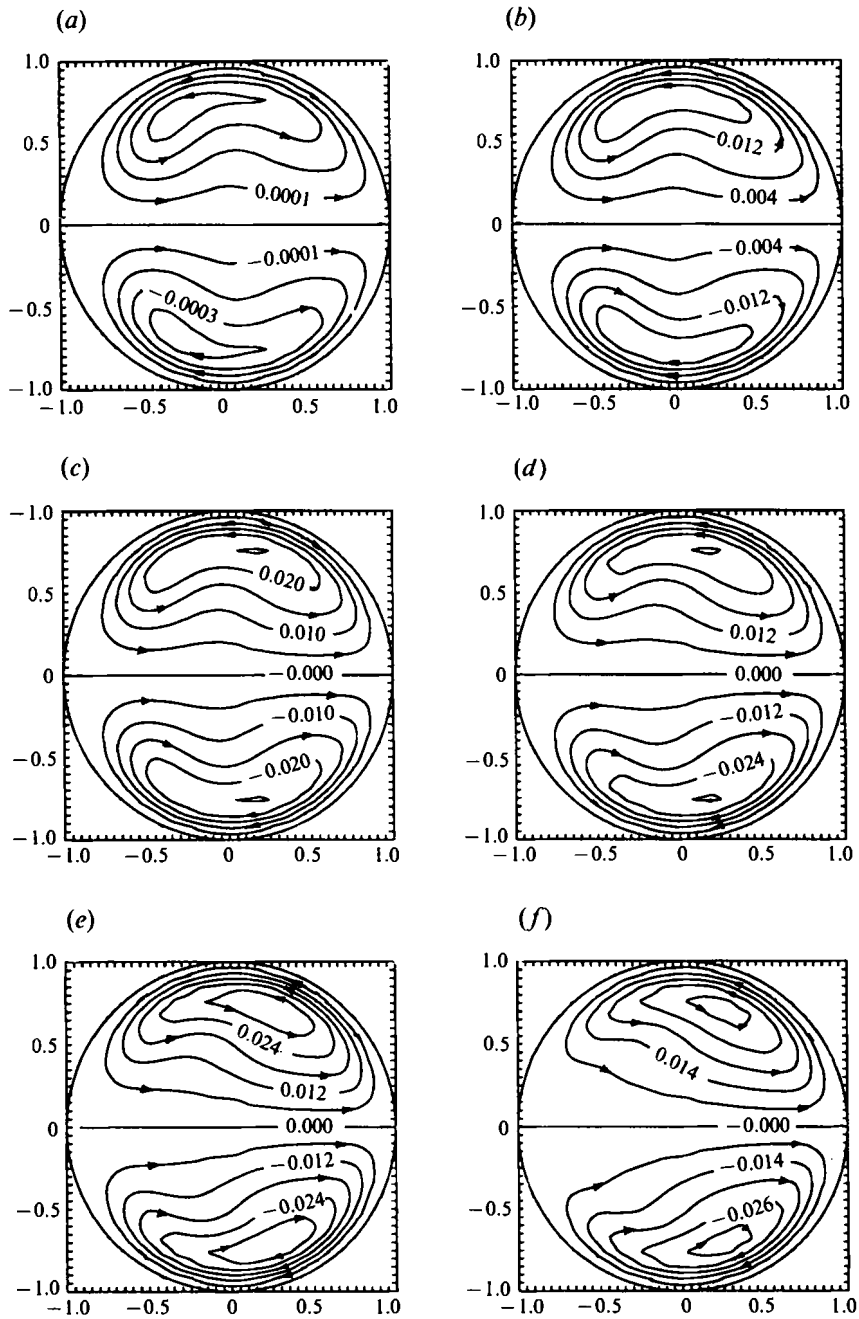

FIGURE 13. Secondary flow patterns for $Dn = 500$ and $\eta = 0$. (*a*) $\lambda = 0.0001$, (*b*) $\lambda = 0.2$, (*c*) $\lambda = 0.4$, (*d*) $\lambda = 0.6$, (*e*) $\lambda = 0.8$, (*f*) $\lambda = 1.0$.

The axial velocity isolines are shown in figure 14 for a very wide range of curvature ratio. For a low value of λ, i.e. when the loose-coiling approximation holds, the axial velocity is characterized by a single maximum velocity value located along the line of symmetry (or more accurately, the vortex dividing line). Its location is close to the outer wall. However, as λ is increased, a case not as yet reported in the literature, the maximum velocity occurs at two locations in the upper and lower section of the torus.

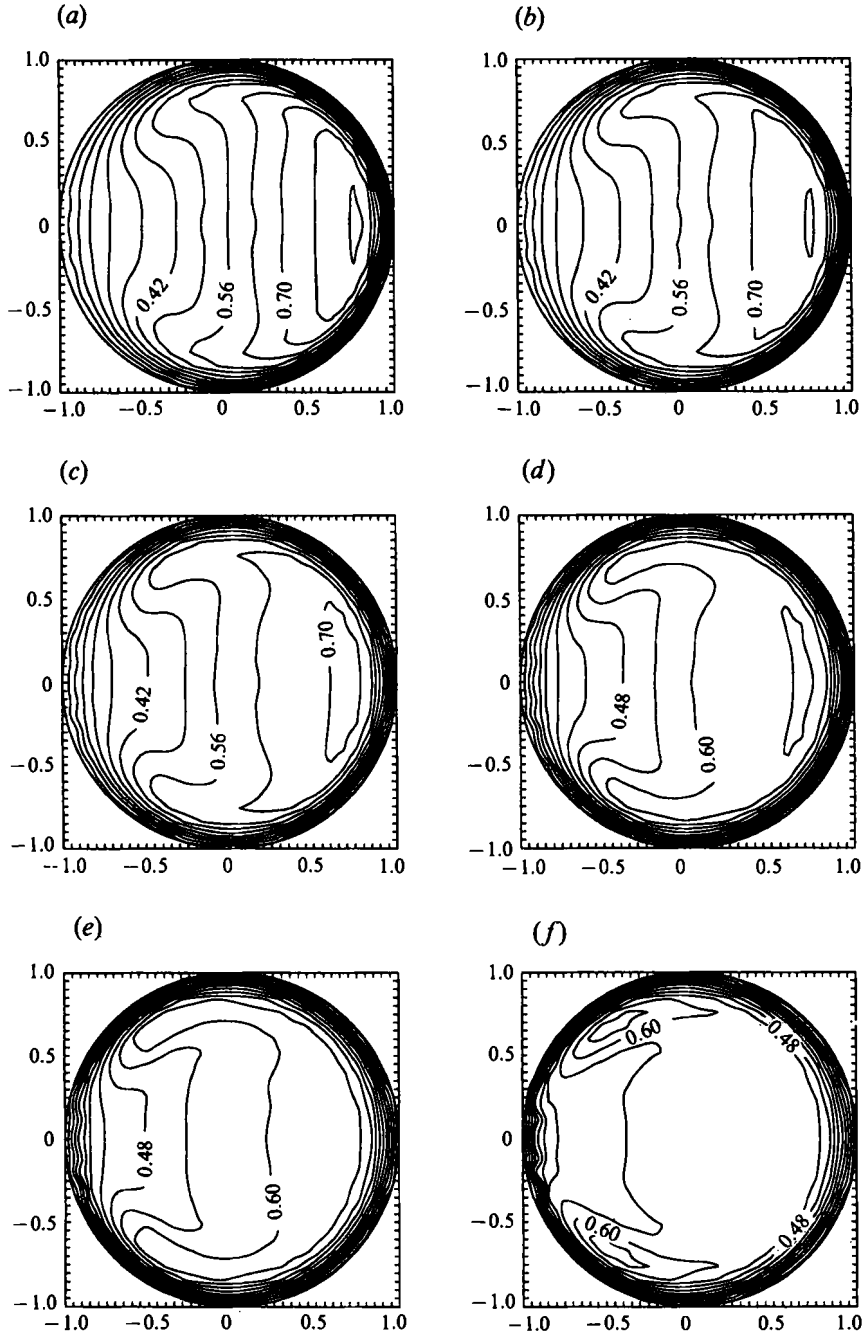

FIGURE 14. Iso-axial velocity contours for $Dn = 500$ and $\eta = 0$. (*a–f*) λ values same as figure 13.

A larger plateau forms around the vortex dividing line as λ is increased. The locations of the maximum axial velocity shift towards the inner wall as λ is increased.

5. Some discussion on the representation of secondary flow

The secondary flow is an important aspect of helical flow behaviour. It determines the fluid movement and the momentum and energy/mass transport in the cross-plane

normal to the axial direction. The rotating secondary flow can also stabilize the helical flow up to a certain extent. Hence, turbulence in helical flow is delayed compared to Poiseuille flow where the secondary flow is absent. Such a stabilizing effect was first observed by Taylor (1929).

Owing to the non-orthogonality of the generic helical coordinate system, difficulty arises in how to view the secondary flow. However, the flow structure is independent of reference frame. Using different reference frames, one may observe different patterns. Hence, there is no right or wrong in presenting the flow in the different reference frames. When viewed from the axial direction parallel to the centreline of the pipe and rotating with the pipe, the secondary flow forms streamtubes. When viewed from the orthogonal axial direction, the secondary flow cannot be presented by streamtubes.

Tuttle (1990) noted that the streamtube is a correct observation in the rotating Frenet frame where the axially invariant (fully developed) flow is extracted. In the limit of small γ, the strength of the true secondary flow may be deduced from the pseudo-secondary flow stream function. Owing to the full circular pipe geometry, no pure torsion effect can be observed (Murata *et al.* 1981; Germano 1989). Hence, the secondary flow strength may not be deduced from the pseudo-secondary flow stream function when γ is large or Gn is dominant. The pure swirling in the cross-section has no influence on the main flow and/or heat-mass transfer characteristics.

On the other hand, the orthogonal secondary velocity is a good indicator of the acting secondary flow at least at both limits of small and large γ. Figures 15(*a*) and 15(*b*) present the secondary flow in the same form as Murata *et al.* (1981), Kao (1987) and Germano (1989). The arrow plots are the orthogonal secondary velocity vectors on the non-orthogonal (r, θ)-plane. The (r, θ)-plane is used to avoid the complication due to the (orthogonal s-) axially variant nature of the helical flow. When the torsion is increased, the secondary flow structure presented in figure 15 is more complicated than that presented in figure 8 for the same flow system.

Figure 15(*a*) shows that the secondary flow consists of two vortices for small γ. When γ increases, the vortex appearance change in the orthogonal coordinate system is the opposite of that in the non-orthogonal coordinate system. An increase in γ for $\gamma < 0.13$ results in the lower vortex gaining both in size and in strength, while figure 8 shows the upper vortex gaining in size and in strength. The change in the vortex structure is relatively abrupt when $\gamma \geqslant 0.04$ as shown in figure 15(*a*).

Figure 15(*b*) is a continuation of figure 15(*a*). The upper vortex becomes very small in figure 15(*b*i,ii) where $\gamma = 0.15$ and 0.185, respectively. Hence we may conclude that the orthogonal secondary flow consists of a one-vortex structure when γ is about 0.16 and Dean number is high. For further increase in γ, the upper vortex starts to gain in size and in strength. The vortex dividing line rotates anticlockwise as γ is increased. When $\gamma = 1$, as shown in figure 15(*b*vi), the two vortices become left and right, and are of nearly the same size and strength.

When γ is large, as shown in figures 15(*b*iv–vi), the orthogonal secondary flow is strong in the centre region and is in the upward direction. In the inner and outer wall regions, the secondary flow is very weak and is in the downward direction. Hence, there is a strong source (coming from the axial flow) located near the lower wall region. A large sink (to the axial flow) appears near the upper wall. This is due to the swirling effect of the axial flow when the twisting forces are dominant. Sinks and sources obscure the representation of the overall fully developed secondary flow.

Figures 16 and 17 show the secondary flow pattern and the orthogonal secondary flow structure for fixed flow rate and radius of coil while varying the pitch of the pipe.

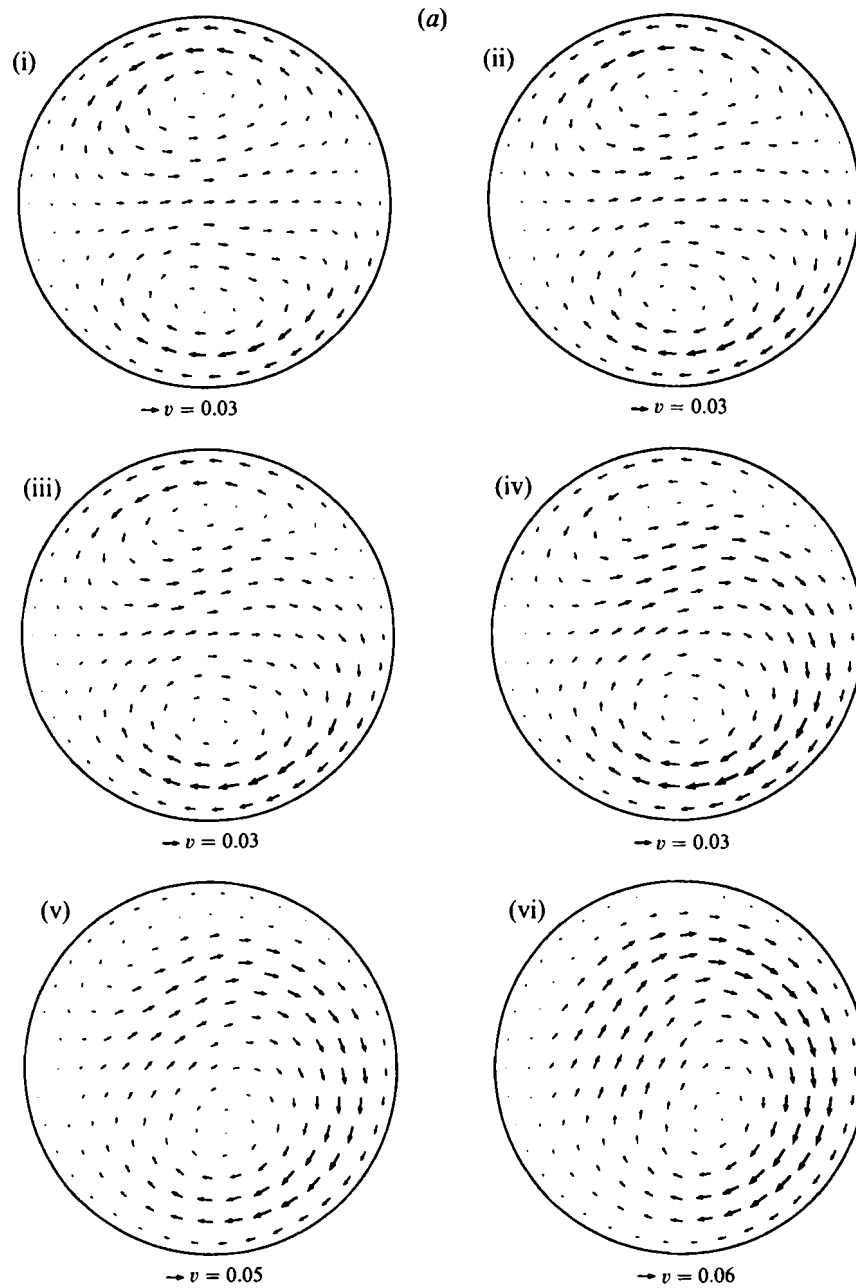

FIGURE 15(*a*). For caption see facing page.

Here, the torsion effect in the small Dean number range can be examined. Figure 16 shows the secondary flow pattern variation with increasing pitch and transition from a two- to a one-vortex pattern. The corresponding orthogonal secondary flow structure, as shown in figure 17, does not show any transition to a one-vortex pattern on increasing the pitch. When the torsion effect is significant (but not dominant), as shown in figure 17(*b*, *c*), the orthogonal secondary flow consists of a strong vortex and a weak vortex. This is in agreement with the observation by Kao (1987). However, when the torsion is dominant, the orthogonal secondary flow structure, figure 17(*e*, *f*),

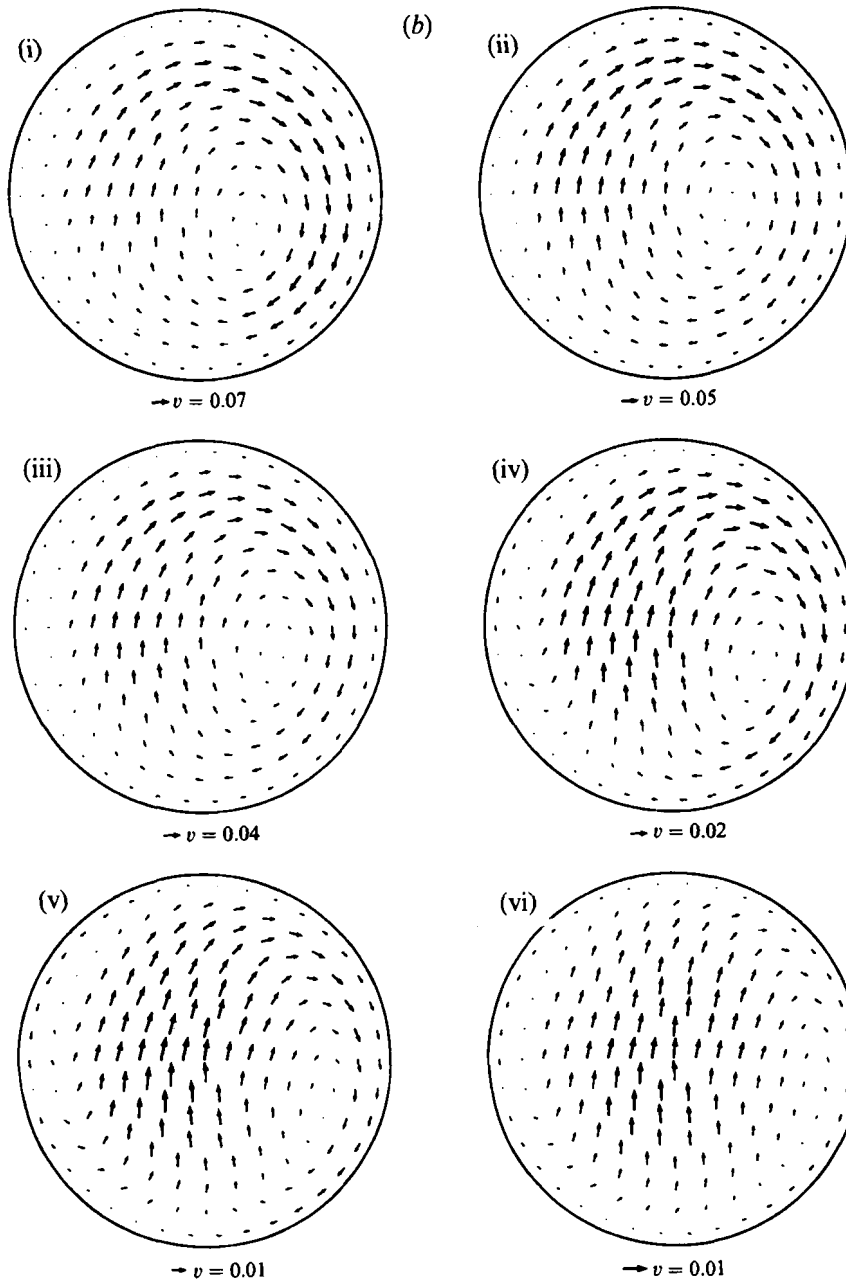

FIGURE 15. Orthogonal secondary flow structure variation with γ for $Dn = 100$, $\lambda = 0.01$, and (*a*) $\gamma \leqslant 0.13$; (i) $\gamma = 0$, (ii) $\gamma = 0.01$, (iii) $\gamma = 0.02$, (iv) $\gamma = 0.04$, (v) $\gamma = 0.08$, (vi) $\gamma = 0.13$. (*b*) $\gamma \geqslant 0.15$: (i) $\gamma = 0.15$, (ii) $\gamma = 0.185$, (iii) $\gamma = 0.22$, (iv) $\gamma = 0.30$, (v) $\gamma = 0.60$, (vi) $\gamma = 1.0$.

looks very similar to the case of the secondary flow in a torus. Since the flow is very weak, the main flow characteristics and transport properties are not influenced by the torsion.

The orthogonal secondary velocity vector plots represent the time-instantaneous secondary flow structure on the (r, θ)-plane. They indicate the direction of the flow normal to the orthogonal axial direction and hence are directly measurable by a pointing device, say, a laser Doppler anemometer. The time-instantaneous direction

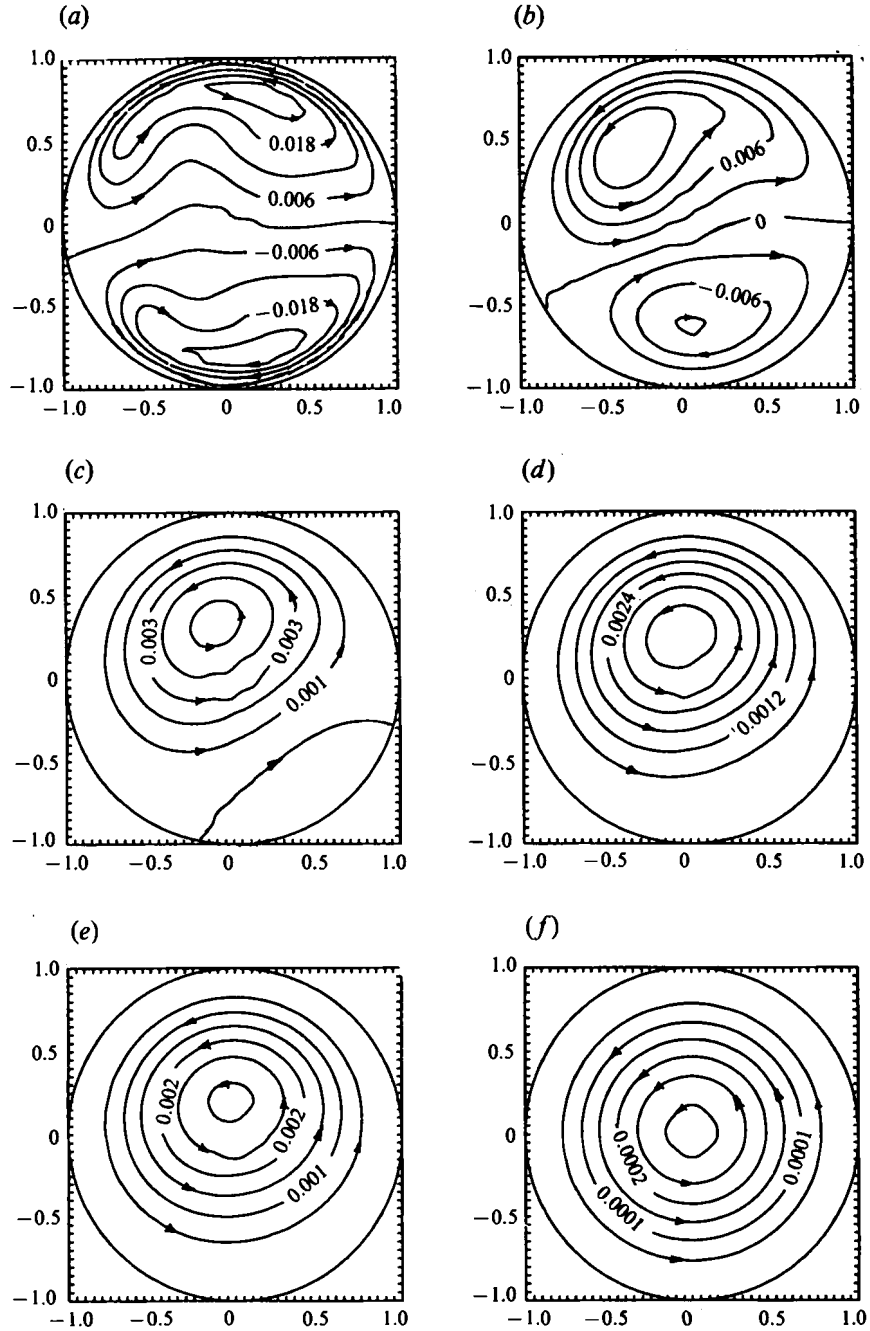

FIGURE 16. Secondary flow pattern variation with changing pitch for fixed $R_c = 1.25$ and $Re = 1000$. (*a*) $H = 5$, $Dn = 754.5$, $\gamma = 0.01749$; (*b*) $H = 50$, $Dn = 138.8$, $\gamma = 0.075$; (*c*) $H = 250$, $Dn = 28.08$, $\gamma = 0.1687$; (*d*) $H = 375$, $Dn = 18.73$, $\gamma = 0.2066$; (*e*) $H = 500$, $Dn = 14.05$, $\gamma^* = 0.06366$; (*f*) $H = 5000$, $Dn = 1.405$, $\gamma^* = 0.6366$.

does not indicate the momentum/energy transport direction on the (r, θ)-plane owing to the geometrical change of the pipe. Hence, the orthogonal secondary flow structure cannot be used to interpret the helical flow behaviour such as friction factor variation without resorting to the secondary flow pattern. Owing to the sources and sinks present

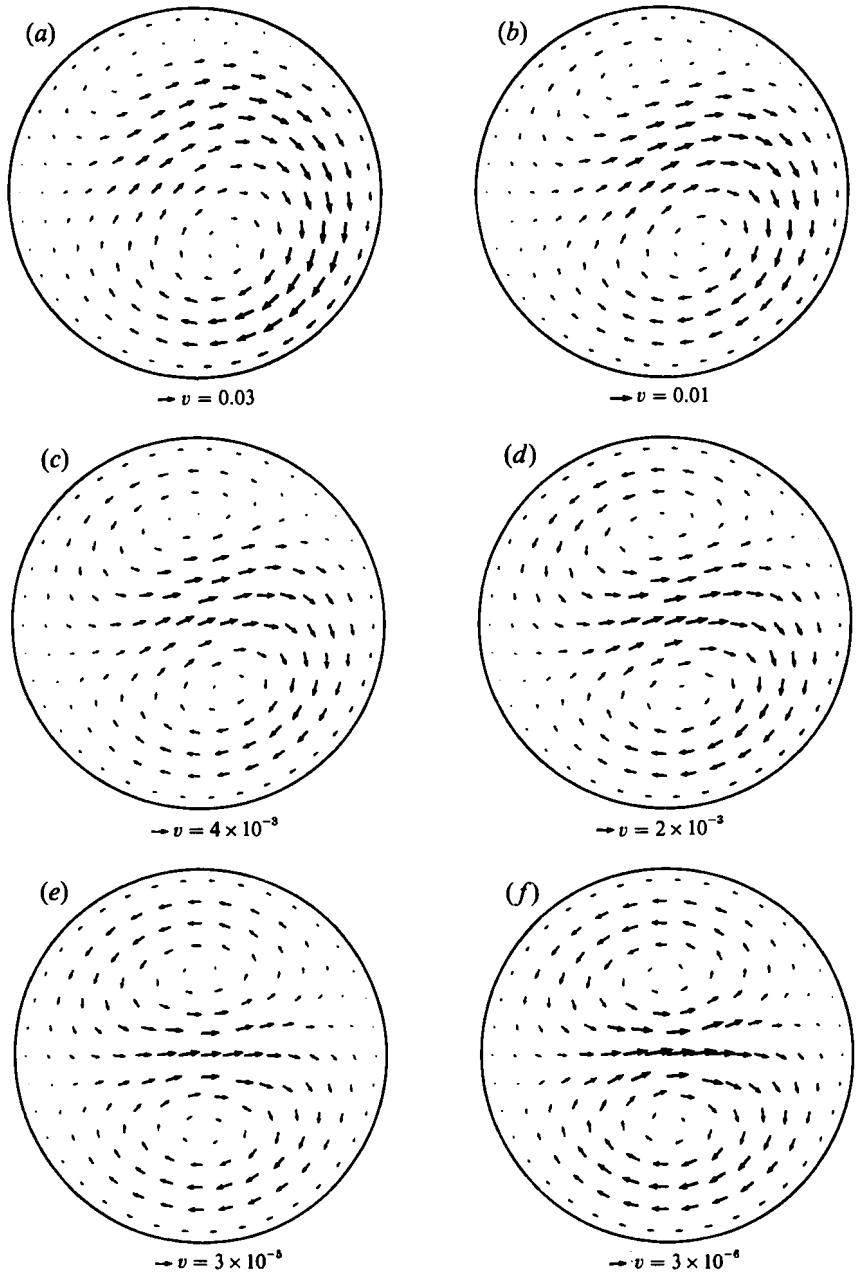

FIGURE 17. Orthogonal secondary flow structure variation with changing pitch for fixed $R_c = 1.25$ and $Re = 1000$. (*a*) $H = 100$, $Dn = 70.03$, $\gamma = 0.1066$; (*b*) $H = 250$, $Dn = 28.08$, $\gamma^* = 0.031\,83$; (*c*) $H = 375$, $Dn = 18.73$, $\gamma^* = 0.047\,75$; (*d*) $H = 500$, $Dn = 14.05$, $\gamma^* = 0.063\,66$; (*e*) $H = 5000$, $Dn = 1.405$, $\gamma^* = 0.6366$; (*f*) $H = 50\,000$, $Dn = 0.1405$, $\gamma^* = 6.366$.

in the orthogonal secondary flow velocity plots for $0 < \gamma < \infty$, they do not represent the overall fluid element movement across the pipe either. However, at the two extremes, $\gamma = 0$ and $\gamma \to \infty$, the arrow plots do represent the true secondary flow. Hence, we may conclude that the orthogonal secondary velocity vector plots should be used with care. They show only part of the secondary flow, mainly the centrifugal force effect.

The secondary flow patterns (pseudo-secondary flow stream function contour plots) represent the s-axis-instantaneous secondary flow structure on the (r, θ)-plane. They are overlapped exposures of secondary flow at various s-distances with the outer wall fixed on the right. The true secondary flow may be diminished by the overwhelmingly large rotation of the axis. Nevertheless, the secondary flow pattern indicates the momentum/energy transport direction on the (r, θ)-plane since the transverse velocity components appear generically in the conservative form of the momentum equations. The transverse velocities (v, ξ) are also directly measurable by, say, measuring the displacement of a marked particle in the generic coordinate system that is easy to locate. Hence, the secondary flow pattern is a property useful in characterizing the helical flow. The secondary flow pattern becomes a valid and accurate representation of the secondary flow if one observes the flow under the rotating non-orthogonal frame. The pseudo-secondary flow stream function isolines can be viewed as a 'tube' such that a fluid particle trapped in the 'tube' will not escape as it moves along the helical pipe (Tuttle 1990). Hence, the secondary flow pattern shows the overall secondary flow appearance, but not the direction of the secondary flow at a given instance. This interpretation of the secondary flow pattern applies equally well to the extreme case of a twisted straight pipe. It can be concluded that the secondary flow pattern is a preferred representation. However, care must also be taken when using the secondary flow pattern (pseudo-secondary flow stream function), that is, one must note that the observation is under the non-orthogonal generic reference frame.

6. Correlation of fRe with Dn, λ and η

Numerous correlations of the friction factor for toroidal flow and/or helical flow under the small pitch limit can be found in the literature (see Nandakumar & Masliyah 1986). However, none of them dealt with helical flow in a pipe of reasonably large pitch. Even the effect of curvature ratio for the case of a torus has not been examined in a wide enough range. To establish formally a suitable correlation, we need to consider the effects of λ and η separately to obtain a correlation equation for the combined effect.

The curvature ratio effect on the friction factor is shown in figures 18(a) and 18(b). In general, it can be observed that the friction factor increases with curvature ratio. For both $Dn = 100$ and 500, the dependence of fRe on λ decreases with increasing λ. However, when $\lambda = \eta$, there is a strong dependence of fRe on λ. Later, it will be shown that fRe is proportional to the square root of λ when Dn is large.

The torsion effect on the friction factor is negligible for commonly used helical coils, where the pitch is usually small compared with the radius of the coil. Some results for the dependence of fRe on γ are shown in figures 19(a) and 19(b). For $Dn = 100$, it can be observed that fRe increases with γ for $\gamma < 0.1$ but otherwise decreases with γ. The increase of fRe with γ can be attributed to the distortion effect of the torsion on the helical flow. As we pointed out, the Germano number causes the secondary flow to be unidirectional through the body-centred azimuthal velocity $\xi = w - \eta ru/h_1$. When λ and Dn are large, $Gn\,\lambda$ and $Gn\,\lambda^2$($\lambda\eta\,Re$ and $\lambda^2\eta\,Re$) become significant. Since these two terms affect the source terms of the secondary flow momentum equations, the flow becomes more complicated as λ and Dn are increased. The complication of the flow causes fRe to rise. As γ is further increased, the twisting forces become dominant and fRe decreases monotonically with further increase in γ.

Since the commonly used helical systems are in the range of $\gamma < 0.1$, we correlate only the first part of the monotonic regions of the friction factor variation with γ. We

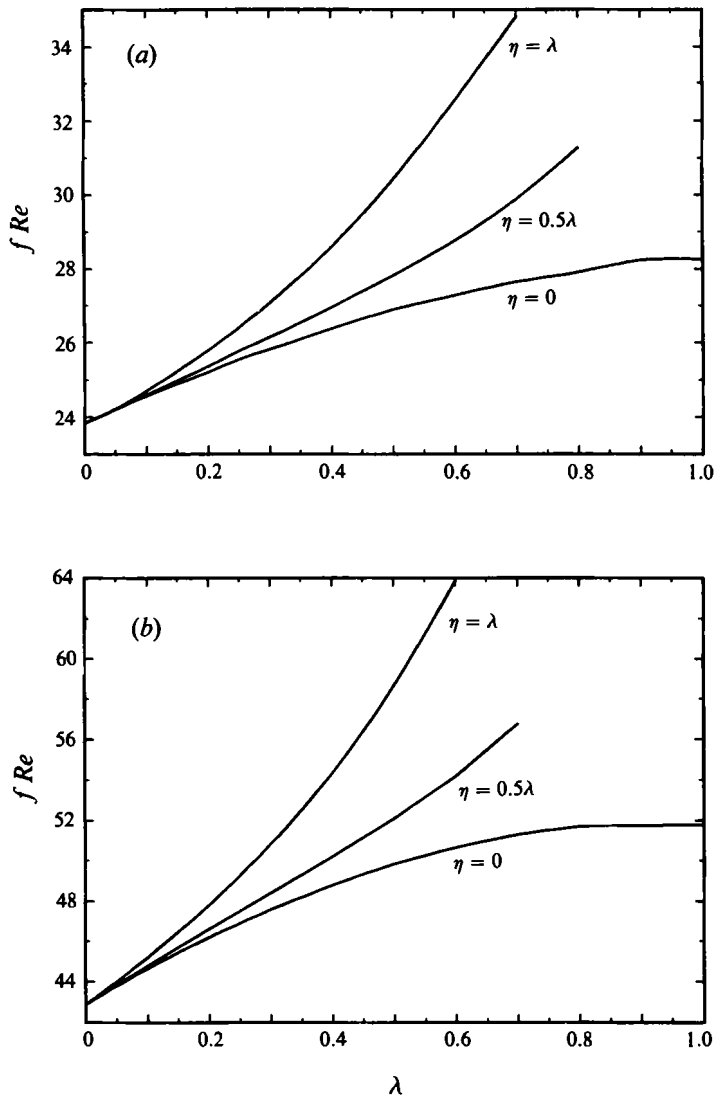

FIGURE 18. Friction factor variation with λ for (*a*) $Dn = 100$, (*b*) $Dn = 500$.

arrive at the following correlation equation which describes the results of over 250 cases for $Dn \leqslant 5000$ and $\gamma < 0.1$:

$$f\,Re = [16 + (0.378\,Dn\lambda^{\frac{1}{4}} + 12.1)\,Dn^{\frac{1}{2}}\lambda^{\frac{1}{2}}\gamma^2] \times \left[1 + \frac{(0.0908 + 0.0233\lambda^{\frac{1}{2}})\,Dn^{\frac{1}{2}} - 0.132\lambda^{\frac{1}{2}} + 0.37\lambda - 0.2}{1 + 49/Dn}\right] \quad (43)$$

with a maximum deviation of less than 2%.

When $\lambda \to 0$, $\gamma \to 0$ and very large $Dn (Dn > 1000)$, the above equation reduces to

$$f\,Re = 16(0.8 + 0.908\,Dn^{\frac{1}{2}}) \quad (44a)$$

or

$$f/f_s = 0.8 + 0.908\,Dn^{\frac{1}{2}}, \quad (44b)$$

where f_s is the friction factor for a straight pipe, i.e. $f_s\,Re = 16$. Equation (44) is in agreement with the literature values as shown in table 7, where a $Dn^{\frac{1}{2}}$ dependence is predicted.

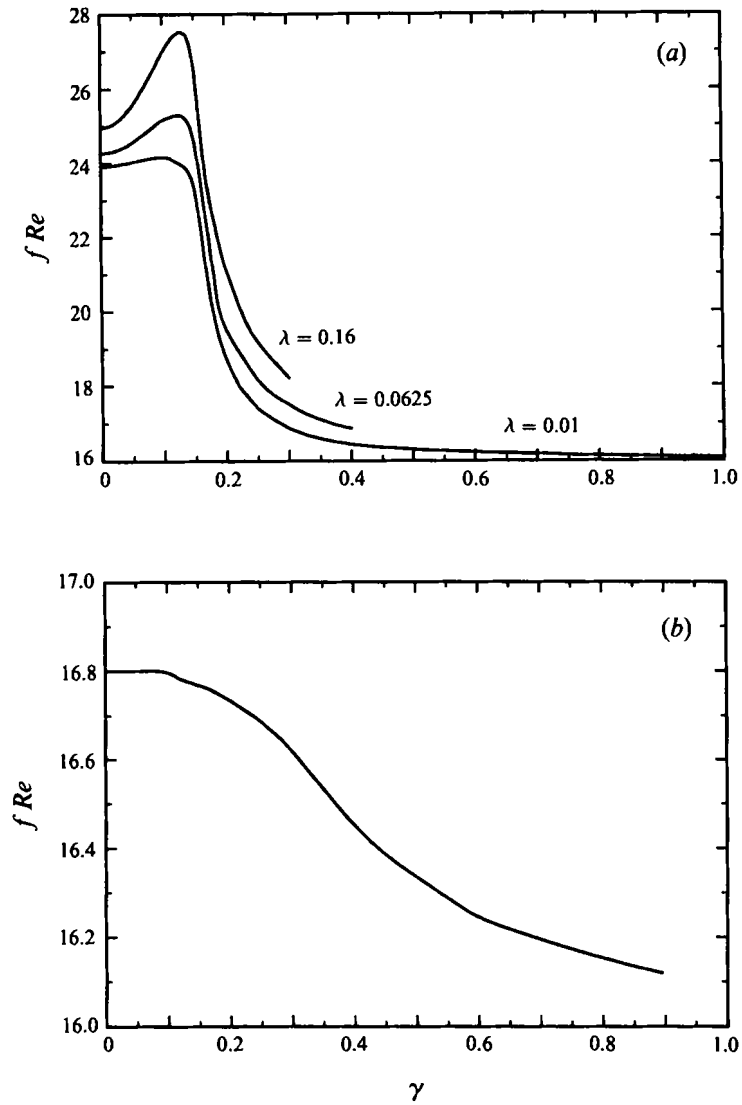

FIGURE 19. Friction factor dependence on the torsion for (*a*) $Dn = 100$ and various λ; (*b*) $Dn = 20$ and $\lambda = 0.0625$.

Equation	Source
$f/f_s = 0.1064 Dn^{\frac{1}{2}}$	Adler (1934)
$f/f_s = 0.509 + 0.0918 Dn^{\frac{1}{2}}$	Barua (1963)
$f/f_s = 0.388 + 0.1015 Dn^{\frac{1}{2}}$	Dennis (1980)
$f/f_s = 0.1033 Dn^{\frac{1}{2}}[(1 + 1.729/Dn)^{\frac{1}{2}} - (1.729/Dn)^{\frac{1}{2}}]^{-3}$	Ito (1969)
$f/f_s = 0.556 + 0.0969 Dn^{\frac{1}{2}}$	Hasson (1955)
$f/f_s = 0.1033 Dn^{\frac{1}{2}}/[1 - 3.253 Dn^{-\frac{1}{2}}]$	Mori & Nakayama (1965)

TABLE 7. Friction factor correlations in the literature in terms of $Dn^{\frac{1}{2}}$

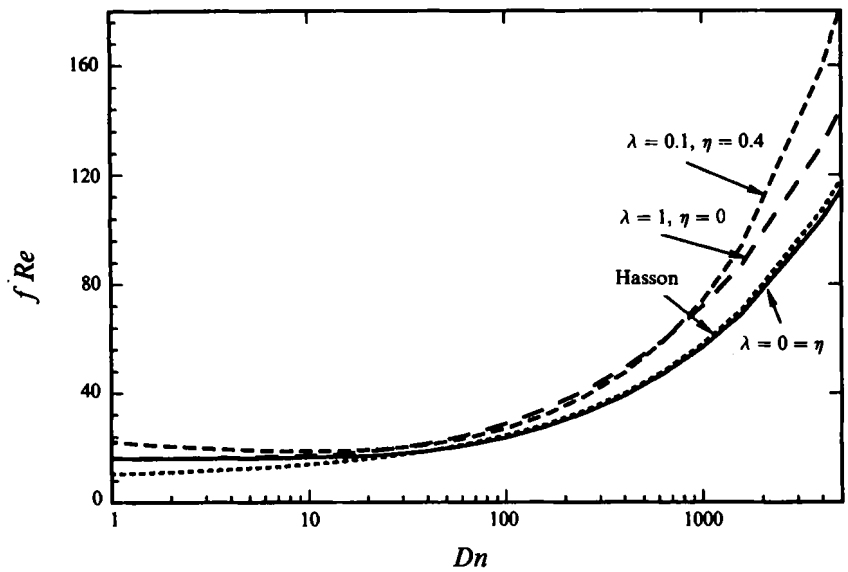

FIGURE 20. The predicted $f\,Re$ curves based on equation (43) and that of Hasson (1955).

Figure 20 shows the predicted $f\,Re$ values using equation (43). As a comparison, the correlation equation by Hasson (1955) for $\lambda \to 0$ and $\eta \to 0$ is also shown. We observe that the friction factor in a helical pipe can be significantly different from that in a torus when torsion and/or curvature ratio is high. The current correlation equation (43) agrees very well with Hasson (1955) in the limiting case of small curvature and negligible torsion for $Dn > 20$.

Equation (43) also shows that there is no pure torsion effect on the friction factor. When zero curvature is imposed, the friction factor in a helical pipe becomes the same as that for a torus. This is in agreement with Murata *et al.* (1981), who specified a zero curvature in the governing equations (except the governing centrifugal force term) and found no torsion effect on the axial pressure drop.

7. Conclusions

Steady fully developed laminar Newtonian flows in helical pipes of a constant circular cross-section with a finite pitch are formulated and numerically studied. The governing flow equations are constructed from orthogonal helical coordinates. They are used to obtain a loose-coiling approximation with two dominant parameters, Dean number, $Dn = Re\,\lambda^{\frac{1}{2}}$, with Reynolds number Re and curvature ratio λ, and Germano number, $Gn = Re\,\eta$, with η being the torsion. The importance of Gn is investigated. For high Dean number flows, a new helical flow group evolves, namely $\gamma = Gn\,Dn^{-\frac{3}{4}} = \eta(\lambda\,Dn)^{-\frac{1}{4}}$. For very small-$Dn$ flows, the counterpart of γ is defined by $\gamma^* = Gn\,Dn^{-2} = \eta/(\lambda\,Re)$. It is further shown that under the loose-coiling conditions and negligible Gn ($\lambda \to 0$, $\gamma \to 0$, and $Re > O(\lambda^{-\frac{1}{2}})$), the helical flow problem reduces to the Dean problem. These qualitative theoretical results are further supported by numerical simulations.

It is found that $f\,Re$ and the flow field profiles are almost invariant with λ and η when Dn is held constant, for $\gamma \leqslant 0.01$ and $\lambda \to 0$. A helical flow may be simplified by a toroidal flow if $\gamma \leqslant 0.01$. With different λ, the cross-plane pressure and the pseudo-secondary flow stream function are proportional to $\lambda^{\frac{1}{2}}$ or Re^{-1} (as are the secondary

velocities) with the contour shapes holding remarkably unchanged. When $\gamma > 0.01$, the flow becomes asymmetric and dependent on Dn and γ only when $\lambda \to 0$ and $\eta \to 0$.

The friction factor increases with increasing torsion when γ is small, especially for large Dean number and large λ. When γ is large, the friction factor decreases sharply towards the value of a straight-pipe Poiseuille flow as γ increases. The friction factor reaches a maximum value at $\gamma \approx 0.1$ for moderate-λ and moderate-Dn flows. But for small Dn and/or small λ, the increase of the friction factor with γ is not apparent. Here, the distortion effect of the torsion on the flow field is minimal. In other words, there is no pure torsion effect on the helical flow.

For large-λ and large-Dn flows, the flow field rotates and distorts as γ increases. The maximum axial velocity increases as the torsion increases, with its location moving spirally from the outer-half of the y-axis towards the centre of the pipe.

The secondary flow pattern or iso-ψ contour plot is the secondary flow structure viewed in the generic (non-orthogonal) coordinate system. When $\gamma > 0.2$ for $Dn \geqslant 20$ or $\gamma^* > 0.039$ for $Dn < 20$, the secondary flow pattern consists of one recirculating vortex, i.e. the helical flow is a swirling flow when viewed in the non-orthogonal coordinate system. When $\gamma < 0.2$ for $Dn \geqslant 20$ or $\gamma^* < 0.039$ for $Dn < 20$, the secondary flow pattern consists of two vortices, that is, the flow is torus-like.

When viewed in the orthogonal coordinate system, the secondary flow is generally of a two-vortex pattern with sources and sinks, except at $\gamma \approx 0.16$ when it is of nearly a one-vortex pattern with a very small vortex at the inner upper wall region. When γ or Dn is small, the two vortices are in an up-and-down position. When γ and Dn are large, the two vortices are left and right. Strong sources and sinks exist in the secondary flow. The existence of sources and sinks indicates that the orthogonal secondary velocity vector plots show only part of the true secondary flow.

A correlation for the friction factor is developed based on the numerical solutions of more than 250 cases. All the controlling parameters Dn, λ and γ are accounted for. For large-Dn flows, the friction factors in the limit of $\lambda \to 0$ and $\eta \to 0$ are in good agreement with previous experimental and numerical observations of $fRe \sim Dn^{\frac{1}{2}}$.

The authors wish to thank the Natural Science and Engineering Research Council of Canada for financial support.

REFERENCES

ADLER, M. 1934 Strömung in gekrümmten Rohren. *Z. Angew. Math. Mech.* **14**, 257–275.

AUSTIN, L. R. & SEADER, J. D. 1973 Fully developed viscous flow in coiled circular pipes. *AIChE J.* **19**, 85–94.

BARUA, S. N. 1963 On secondary flow in stationary curved pipes. *Q. J. Mech. Appl. Maths* **16**, 61–77.

BERGER, S. A. 1991 Flow and heat transfer in curved pipes and tubes. *AIAA* 91-0030.

CHADWICK, R. S. 1985 Slow viscous flow inside a torus – the resistance of small tortuous blood vessels. *Q. Appl. Maths* **43**, 317–323.

DASKOPOULOS, P. & LENHOFF, A. M. 1989 Flow in curved ducts: bifurcation structure for stationary ducts. *J. Fluid Mech.* **203**, 125–148.

DEAN, W. R. 1927 Note on the motion of fluid in a curved pipe. *Phil. Mag. J. Sci.* **4**, 208–223.

DEAN, W. R. 1928 The stream-line motion of fluid in a curved pipe. *Phil. Mag. J. Sci.* **5**, 673–695.

DENNIS, S. C. R. 1980 Calculation of the steady flow through a curved tube using a new finite difference method. *J. Fluid Mech.* **99**, 449–467.

DENNIS, S. C. R. & NG, M. 1982 Dual solutions for steady laminar flow through a curved tube. *Q. J. Mech. Appl. Maths* **35**, 305–324.

GERMANO, M. 1982 On the effect of the torsion in a helical pipe flow. *J. Fluid Mech.* **125**, 1–8.

GERMANO, M. 1989 The Dean equations extended to a helical pipe flow. *J. Fluid Mech.* **203**, 289–305.

HASSON, D. 1955 Streamline flow resistance in coils. *Res. Correspondence*, **1**, s1.

ITO, H. 1969 Laminar flow in curved pipes. *Z. Angew. Math. Mech.* **11**, 653–663.

KAO, H. C. 1987 Torsion effect on fully developed flow in a helical pipe. *J. Fluid Mech.* **184**, 335–356.

LIU, S. 1992 Laminar flow and heat transfer in helical pipes with a finite pitch. PhD dissertation, University of Alberta, Edmonton, Canada.

LIU, S. & MASLIYAH, J. H. 1993 A decoupling numerical method for fluid flow. *Intl J. Numer. Meth. Fluids* (in press).

MANLAPAZ, R. & CHURCHILL, S. W. 1980 Fully developed laminar flow in a helically coiled tube of finite pitch. *Chem. Engng Commun.* **7**, 57–58.

MORI, Y. & NAKAYAMA, W. 1965 Study on forced convective heat transfer in curved pipes. *Intl J. Heat Mass Transfer* **8**, 67–82.

MURATA, S., MIYAKA, Y., INABA, T. & OGATA, H. 1981 Laminar flow in a helically coiled pipe. *Bull. JSME* **24**, 355–362.

NANDAKUMAR, K. & MASLIYAH, J. H. 1982 Bifurcation in steady laminar flow through curved tubes. *J. Fluid Mech.* **119**, 475–490.

NANDAKUMAR, K. & MASLIYAH, J. H. 1986 Swirling flow and heat transfer in coiled and twisted pipes. In *Advances in Transport Processes*, vol. IV (ed. A. S. Mujumdar & R. A. Mashelkar). Wiley Eastern.

TAYLOR, G. I. 1929 The criterion for turbulence in curved pipes. *Proc. R. Soc. Lond.* A **124**, 243–249.

TRUESDELL, L. C. & ADLER, R. J. 1970 Numerical treatment of fully developed laminar flow in helically coiled tubes. *AIChE J.* **16**, 1010–1015.

TUTTLE, E. R. 1990 Laminar flow in twisted pipes. *J. Fluid Mech.* **219**, 545–570.

VAN DYKE, M. 1990 Creeping flow in a coiled pipe by computer-extended series. In *Yung-huai Kuo Memorial Volume* (ed. Zheng *et al.*), p. 35. Beijing: Science Publishing Co.

WANG, C. Y. 1981 On the low-Reynolds-number flow in a helical pipe. *J. Fluid Mech.* **108**, 185–194.

XIE, D. G. 1990 Torsion effect on secondary flow in a helical pipe. *Intl J. Heat Fluid Flow* **11**, 114–119.

YANASE, S., GOTO, N. & YAMAMOTO, K. 1989 Dual solutions of the flow through a curved tube. *Fluid Dyn. Res.* **5**, 191–201.

YANG, Z. & KELLER, H. B. 1986 Multiple laminar flows through curved pipes. *Appl. Numer. Maths* **2**, 257–271.